https://doi.org/10.5194/egusphere-2026-6536
Preprint. Discussion started: 22 November 2026
© Author(s) 2026. CC BY 4.0 License.

Spatiotemporal Dynamics and Environmental Drivers of CO_2 Fluxes in Typical Qinghai–Tibet Alpine Ecosystems

Shengchun Wang1,2,3 , Zhen Qiao1,2,3,*,† , Wenwen Bai1,2,3,†, Zhuolun He4, Wende A4, Xin Li4, Wenhui Li4, Xinyimiao Zhang1, Qingliang Zeng1, Qinxia Zhao1,2,3

1. School of Civil and Hydraulic Engineering, Qinghai University, Xining 810016, China
2. Laboratory of Ecological Protection and High-Quality Development in the Upper Yellow River, Xining 810016, China
3. Key Laboratory of Water Ecological Governance and Protection in River Source Regions, Ministry of Water Resources, Xining 810016, China
4. Qinghai Provincial Hydrology and Water Resources Survey Center, Xining 810000, China

† These authors contributed equally to this work.

Correspondence to: Zhen Qiao (2023990049@qhu.edu.cn)

Abstract. Alpine ecosystems on the Qinghai–Tibet Plateau hold vast carbon stocks, yet how carbon exchange differs among coexisting ecosystem types, and what controls these differences, remains poorly constrained, limiting regional carbon-budget assessment. Here we analyse continuous eddy covariance measurements from June 2021 to March 2025 at three typical ecosystems in the Three-River Headwaters region (TRHR): an alpine meadow (CMR), a lakeside meadow (ZLH), and an alpine wetland (CDX). Combining clearness-index weather typing, Michaelis–Menten light-response modelling, bin-averaged response curves, piecewise regression threshold detection, and a multi-model importance scoring framework validated by five weighting schemes and Monte Carlo perturbations, we resolve net ecosystem CO_2 exchange (*NEE*) dynamics from diurnal to interannual scales. The three ecosystems share a highly synchronized seasonal rhythm – a strong summer sink, a weak winter sink, and transitional spring and autumn – but diverge fundamentally in carbon function: CMR and ZLH acted as persistent net carbon sinks (multi-year mean *NEE* of -0.85 and -0.59 μmol $CO_2 \cdot m^{-2} \cdot s^{-1}$), whereas CDX was a net annual carbon source (0.11 μmol $CO_2 \cdot m^{-2} \cdot s^{-1}$; cumulative 153.2 g C m^{-2}), with no significant long-term trend at any site over the short record. Cloud cover enhanced carbon uptake at all sites, but only within a moderate radiation window (photosynthetically active radiation, *PAR*, of 500–750 μmol $\cdot m^{-2} \cdot s^{-1}$), revealing a light-intensity-dependent diffuse-radiation fertilization effect. *NEE* responded nonlinearly to environmental forcing, with robust response thresholds for *PAR* (683.50–803.73 μmol $\cdot m^{-2} \cdot s^{-1}$), vapour pressure deficit (391.99–440.92 Pa), and soil temperature (9.61–11.45 °C), whereas soil water content explained little and air-temperature thresholds were significant only at CDX and ZLH. A day-night regulatory switch governed the controls – radiation dominated daytime *NEE*, whereas temperature dominated at night – producing three site-level driving regimes with contrasting climate sensitivities: temperature-dominated and warming-vulnerable at CMR, multi-factor synergistic regulation led by *TA* at CDX, and purely radiation-limited at ZLH. These results provide a first synchronized multi-ecosystem flux benchmark for the TRHR and indicate that ecosystem type, rather than climate trend, currently differentiates alpine carbon source–sink functions.

https://doi.org/10.5194/egusphere-2026-6536
Preprint. Discussion started: 22 November 2026
© Author(s) 2026. CC BY 4.0 License.

1 Introduction

The terrestrial carbon cycle is central to global climate change research, and climate-sensitive alpine ecosystems dominate regional carbon budgets (Pepin et al., 2015). Known as the "Third Pole" and "Asian Water Tower", the Tibetan Plateau contains extensive alpine grasslands and permafrost with huge soil carbon reservoirs; permafrost soil organic carbon alone reaches tens of petagrams (Ding et al., 2016), endowing the plateau with a pivotal role in global carbon cycling (Yao et al., 2019, 2022). Although alpine vegetation has low areal productivity, its wide coverage strongly modulates regional and global carbon budgets (Fang et al., 2010; Huang et al., 2023). Over the past five decades, the Tibetan Plateau has warmed at nearly twice the global average rate (Chen et al., 2015). Warming exerts dual controls on alpine carbon cycles: it extends the growing season and enhances photosynthetic carbon uptake, while permafrost thaw accelerates soil organic carbon decomposition and strengthens soil carbon emissions (Han, 2019; **Schädel** et al., 2016). The trajectory and stability of alpine carbon source–sink dynamics under warming remain controversial, and their underlying mechanisms are still unclear (Wang and Piao, 2023). Long-term in situ flux observations characterizing alpine CO_2 exchange and environmental controls are therefore critical for improving regional carbon cycle understanding and robustly evaluating alpine ecosystem responses to climate change.

NEE, regulated by gross primary productivity (*GPP*) and ecosystem respiration (*RECO*), is a key indicator of ecosystem carbon source–sink functions (Chapin et al., 2002). *GPP* represents vegetation photosynthetic carbon uptake, while *RECO* combines plant autotrophic and soil microbial heterotrophic respiration; their dynamic balance dominates the spatiotemporal variation of *NEE*. As a continuous and non-destructive in-situ monitoring method, the eddy covariance technique has been widely applied to alpine carbon flux observations (Xiao et al., 2026). Alpine *NEE* exhibits distinct multi-temporal variations: diurnally, ecosystems uptake carbon during the day and release carbon at night, with midday photosynthetic inhibition under strong light conditions (Wang et al., 2021); seasonally, carbon sequestration concentrates in the growing season, and water and temperature jointly control vegetation phenology and grassland carbon flux dynamics (He et al., 2025); interannually, warming, drought and freeze–thaw cycles cause divergent environmental sensitivities of *GPP* and *RECO*, driving nonlinear carbon cycle variations (Wang et al., 2021; Wei et al., 2022). Although multi-site flux data have revealed spatial carbon flux patterns (Wei et al., 2021), most studies focus on single-site observations. Large-scale carbon assessments mainly depend on remote sensing and model simulations, which fail to disentangle the drivers of spatial carbon differentiation and restrict the mechanistic understanding of regional alpine carbon cycling (Chen et al., 2022).

Located in the hinterland of the Tibetan Plateau, the TRHR covers typical alpine meadow, lakeside meadow, and alpine wetland ecosystems, providing an ideal platform for comparative research on alpine carbon cycling (Sun et al., 2012; Zeng et al., 2023). Alpine meadows, the dominant regional vegetation type, are hydrothermally limited and serve as the primary carbon sink in this region (Wang et al., 2023). Lakeside meadows benefit from lake water supplementation with higher soil moisture and reduced drought stress, though low temperatures at high elevations strongly constrain photosynthetic carbon uptake (Li et al., 2012). Alpine wetlands possess abundant soil carbon reserves and favorable hydrological conditions with great carbon sequestration potential (Sun et al., 2025); nevertheless, current studies primarily focus on wetland carbon emissions, while the nonlinear and multi-factor regulatory mechanisms of net carbon exchange remain poorly understood (He et al., 2022). These three ecosystems exhibit distinct vegetation, soil and hydrological properties and spatially differentiated carbon exchange characteristics. However, synchronous multi-ecosystem comparisons based on unified in-situ observations are still insufficient, and the divergent mechanisms governing their carbon cycles remain unclear. At the regional scale, remote-sensing-derived net ecosystem productivity indicates that the Three-River Headwaters region functions predominantly as a carbon sink with prominent southeast-northwest spatial gradients (Zhang et al., 2023). However, multi-ecosystem synchronous in-situ flux observations are still insufficient to unpack fine-scale local regulatory mechanisms behind such large-scale spatial heterogeneity.

Solar radiation governs vegetation carbon uptake, and *PAR*, *TA*, *TS*, *SWC* and *VPD* are key regulators of *NEE* in alpine ecosystems (Wang et al., 2016; Wei et al., 2022). Light exerts threshold controls on photosynthesis: low light limits carbon

https://doi.org/10.5194/egusphere-2026-6536
Preprint. Discussion started: 22 November 2026
© Author(s) 2026. CC BY 4.0 License.

assimilation, and light exceeding saturation induces photoinhibition (Shi et al., 2013). The enhanced carbon uptake under diffuse radiation has been confirmed in forests and Chinese plantations (Gu et al., 2002; Liu et al., 2014), yet this effect is ecosystem-specific. Alpine ecosystems have short canopies and low leaf area indices; how sunny–cloudy conditions and radiation composition modulate their carbon exchange, and divergent responses across ecosystem types, remain poorly quantified (Jung et al., 2017). Temperature and moisture jointly modulate carbon cycling via photosynthetic and microbial activity: low temperature suppresses photosynthesis, while warming increases respiratory carbon loss (Zhang et al., 2012; Li et al., 2020). Soil water exerts bidirectional controls on *NEE*: drought causes stomatal closure and reduced carbon uptake, and waterlogging triggers anaerobic root stress (Souza et al., 2004; Wang et al., 2024); high *VPD* also induces stomatal closure and inhibits photosynthesis (Liu et al., 2024). Most prior studies focus on linear *NEE* responses to environmental drivers. Although nonlinear and threshold behaviours of alpine carbon fluxes have been documented (Wang et al., 2021; He et al., 2025), quantitative threshold analyses remain limited, impeding robust identification of environmental ranges controlling carbon flux dynamics (Wang and Piao, 2023).

In summary, current TRHR alpine carbon-cycle research has four key limitations. First, single-site observations cannot separate local environmental noise; synchronous multi-ecosystem comparisons are lacking, masking dominant drivers of spatial carbon flux divergence. Second, studies prioritize seasonal and interannual variations while neglecting fine-scale short-term controls, notably sunny–cloudy shifts and radiation composition. Third, traditional linear methods dominate, with few quantitative estimates of nonlinear *NEE* responses and environmental thresholds. Fourth, most do not separate photosynthesis-driven daytime signals from respiration-integrated daily *NEE* averages, leaving temporal heterogeneity in regulatory mechanisms unresolved. Collectively, these gaps hinder mechanistic understanding of divergent carbon cycling across TRHR alpine ecosystems.

To fill these gaps, this study examined multi-temporal *NEE* dynamics and environmental controls across three TRHR alpine ecosystems (alpine meadow, lakeside meadow, alpine wetland) using consistent eddy covariance records and standardized data processing. Three core questions were addressed: (1) How do diurnal, seasonal and interannual *NEE* dynamics converge and diverge across sites? (2) Do sunny–cloudy radiation differences yield consistent *NEE* responses among ecosystems? (3) Do environmental factors control *NEE* through nonlinear thresholds, and do such mechanisms differ spatially? This study reveals divergent carbon source–sink behaviours of these alpine ecosystems, supplying observational and theoretical support for regional ecological protection and reliable carbon budget assessment.

2 Materials and methods

2.1 Study area

Three eddy covariance sites were deployed in the core protected area of the Three-River Headwaters region (Fig. 1): Chumar River alpine meadow (CMR), Zhaling Lake lakeside meadow (ZLH), and Chadan alpine wetland (CDX), representing the Yangtze, Yellow and Lancang River source regions, respectively. CMR is dominated by Carex (Li et al., 2024); ZLH is covered by Kobresia meadow (Duan et al., 2024); CDX features Kobresia peat–marsh wetland (Yang et al., 2025). These three sites capture typical alpine meadow, lakeside meadow and alpine wetland, and represent carbon cycle spatial divergence across TRHR source basins (Table A1).

https://doi.org/10.5194/egusphere-2026-6536
Preprint. Discussion started: 22 November 2026
© Author(s) 2026. CC BY 4.0 License.

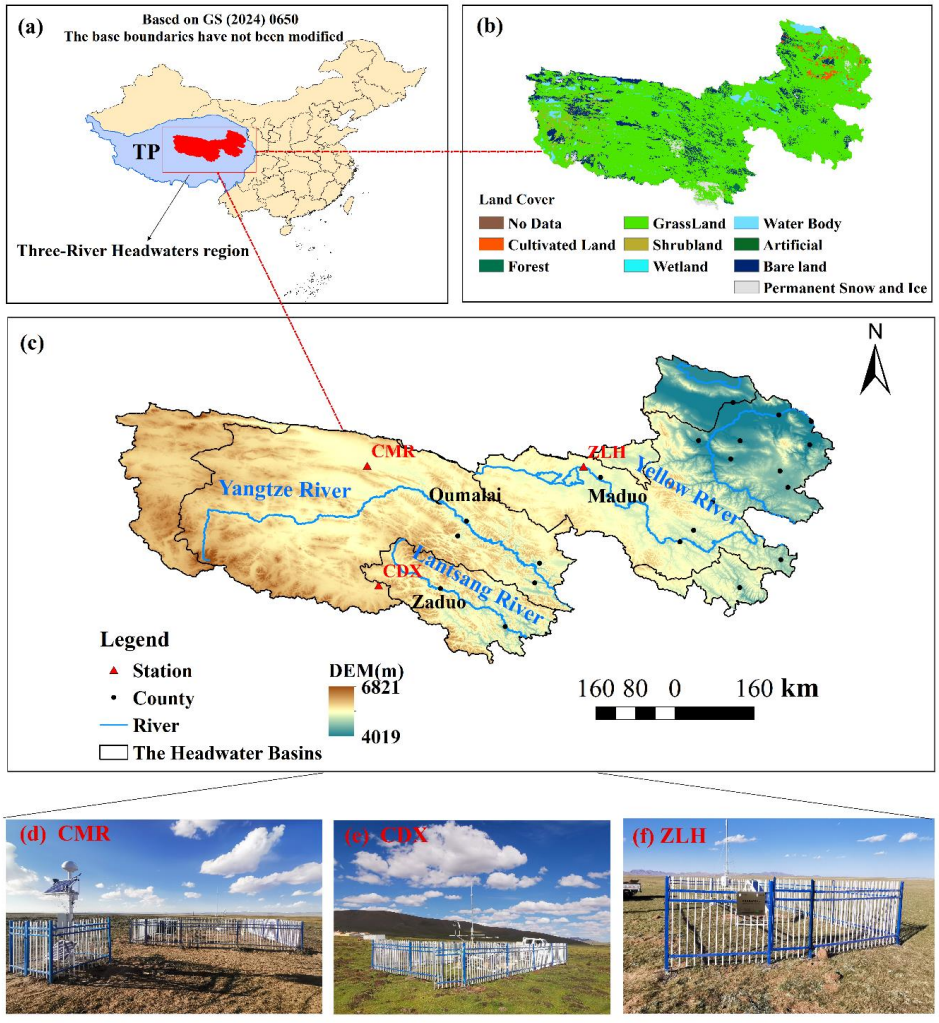


Figure 1. Basic characteristics of the study area: (a) location sketch map; (b) land cover distribution; (c) topography and geographical location; (d) CMR flux site; (e) CDX flux site; and (f) ZLH flux site. TP denotes the Qinghai–Tibetan Plateau.

The region exhibits a plateau continental climate with strong solar radiation (~6000 MJ·m^{-2} annual total). Mean annual air temperature ranges −5.6 to 3.8 °C, and annual precipitation 200–800 mm, with 83% occurring from May to September (Qian et al., 2021; Zeng et al., 2023); the main growing season extends from May to September (Xie et al., 2022). Alpine meadows and alpine steppes dominate vegetation, covering 58% and 24% of the region, respectively (Li et al., 2025).

2.2 Eddy covariance and meteorological measurements

Open-path eddy-covariance systems were deployed at all three sites. Each setup included a WindMaster Pro 3D sonic anemometer (Gill Instruments, UK) and an open-path CO_2/H_2O gas analyzer(LI-7500), measuring turbulent ecosystem–atmosphere CO_2 and water vapor fluxes (Baldocchi, 2003). Instruments were mounted at 2 m height; raw high-frequency data were sampled at 10 Hz to record 3D wind velocity, CO_2 and water vapor concentrations. Collocated biometeorological sensors measured *PAR*, *TA*, *TS*, *SWC*, and relative humidity (*RH*); *VPD* was calculated from *TA* and *RH*. Limited by field power, instrument maintenance and extreme weather, cross-site comparisons used overlapping observation periods to guarantee consistency, while single-site time-series analyses adopted all valid site-specific records.

https://doi.org/10.5194/egusphere-2026-6536
Preprint. Discussion started: 22 November 2026
© Author(s) 2026. CC BY 4.0 License.

2.3 Flux data processing and quality control

Raw high-frequency flux data were processed using EddyPro v7.0.9 (LI-COR), with coordinate rotation, time-lag compensation, *WPL* air-density and frequency-response corrections, to derive 30-min *NEE*. The sign convention follows: *NEE* < 0 indicates ecosystem CO_2 uptake, and *NEE* > 0 indicates CO_2 release to the atmosphere.

Flux data quality control was conducted regarding turbulence, precipitation interference, physiological rationality, and numerical outliers. The u* threshold was dynamically determined by temperature binning to remove low-turbulence invalid observations (Wutzler et al., 2018). Precipitation-affected flux records contaminated by water vapor and raindrops were removed (Foken et al., 2012). Physiologically unrealistic nighttime false carbon sinks (*PAR* < 10 μmol·m^{-2}·s^{-1}) were filtered out to eliminate spurious values while retaining valid respiratory signals (Aubinet et al., 2012). Additional numerical thresholds were used to screen extreme outliers (Li et al., 2005).

Quality-controlled flux gaps were filled by a segmented scheme: linear interpolation for gaps ≤ 2 h, for long gaps exceeding 2 h, a random forest (RF) model was constructed using all high-quality synchronous site observations for gap filling (`Pillai` et al., 2026). Predictors included *PAR*, *TA*, *VPD*, *SWC*, *TS*, rain and day of year (DOY). To avoid extrapolation risk, random forest (RF) prediction was only performed for missing periods where environmental predictors fell within the range of training samples; long gaps outside this range were retained as missing (Abdaki et al., 2025; Xie, 2014; Hou et al., 2025). After quality control and before gap-filling, all statistics were derived from the original half-hourly records. The overall missing fraction, pooled across the three sites, was 29.95% (25.49% at CMR, 34.06% at CDX and 29.14% at ZLH). Missing records were concentrated in gaps lasting several hours: gaps of 3.5 h to 1 d (7–48 consecutive half-hourly records) contained 54.07% of all missing records, gaps of 1–3 h (2–6 records) 37.38%, and isolated single half-hourly records (0.5 h) the remaining 8.55% (Table A2). No gap exceeded one day at any site, and the longest continuous gap (19.5 h, at ZLH) was accompanied by maxima of 15.5 h at CDX and 13.0 h at CMR. The final dataset therefore supports analyses at multiple timescales and mechanism interpretation.

2.4 Multi-timescale analysis of *NEE* dynamics

2.4.1 Clearness index and sky-condition classification

To explore divergent *NEE* responses to radiation under sunny and overcast conditions, we classified weather types using the clearness index (CI): CI ≥ 0.70 represents sunny conditions, CI ≤ 0.35 represents cloudy conditions; transitional samples with $0.35 < CI < 0.70$ were excluded (Chen et al., 2018). Only the moderate *PAR* bin of 500–750 μmol·m^{-2}·s^{-1} with sufficient samples was used for grouped tests. Welch's t-test, appropriate for samples with unequal variances, was adopted to determine the significance of *NEE* differences between sunny and cloudy groups within each identical *PAR* bin. The formula for *CI* is given below:

$$CI = \frac{SW_{in}}{SW_0} \quad (1)$$

SW_{in}: measured downward shortwave radiation at the surface (W·m^{-2});

SW_0: theoretical clear-sky shortwave radiation, computed from site latitude/longitude, elevation, and the half-hourly timestamp using the Ineichen clear-sky model implemented in the Python pvlib library (version 0.15.2) (W·m^{-2}).

2.4.2 Diurnal, seasonal, and monthly analyses

Multi-timescale *NEE* dynamics were analysed using gap-filled 30-min flux records. For diurnal patterns, peak growing-season data (July–August 2023) were used to derive composite sunny/cloudy diurnal *NEE* curves, and daily carbon budgets were calculated via flux integration.

Seasons followed Northern Hemisphere meteorological definitions; the regional growing season was May–September. Monthly and seasonal *NEE* variations were compared across the three ecosystems. Long-term trends of monthly *NEE* and

https://doi.org/10.5194/egusphere-2026-6536
Preprint. Discussion started: 22 November 2026
© Author(s) 2026. CC BY 4.0 License.

environmental drivers were quantified using the Mann–Kendall test with Sen's slope, with pre-whitening to eliminate serial autocorrelation. Cumulative *NEE* time series were generated to track total carbon sequestration. Standardized anomalies (baseline: multi-year monthly mean; threshold: ±2 SD) identified anomalous carbon-budget months, and cumulative anomaly analysis detected turning points in carbon source/sink status.

2.5 STL decomposition of environmental factor time series

Daily environmental variables (*PAR, VPD, SWC, TA, TS*) were decomposed into seasonal, trend and residual components via *STL* (seasonal-trend decomposition using Loess). Uniform settings were adopted: 365-d seasonal period, seasonal smoothing window(a moving-window size of 7 data points), trend smoothing window (a moving-window size of 13 data points), and robust mode activated. Linear regression on trend components yielded long-term slopes and R^2 for each variable; seasonal amplitude was calculated as seasonal maximum minus minimum. Boxplots of these variables were generated across four meteorological seasons.

2.6 Single-factor nonlinear responses and threshold identification

2.6.1 Michaelis–Menten light-response model

Given the rapid photosynthetic saturation and weak photoinhibition of alpine ecosystems, we fitted the simplified Michaelis–Menten model (Falge, 2001) to growing-season daytime flux data to quantify *NEE–PAR* responses across the three ecosystems. This parsimonious model avoids over-parameterization and captures alpine carbon uptake and light-saturation features. The model is formulated as follows:

$$NEE = \frac{\alpha F_{max} \times PAR}{F_{max} + \alpha PAR} \quad (2)$$

where α is the apparent quantum efficiency (μmol CO_2·μmol^{-1} photons) and F_{max} represents light-saturated net ecosystem CO_2 exchange (μmol $CO_2 \cdot m^{-2} \cdot s^{-1}$). Parameters were fitted separately per site; the light-saturation point was derived from *NEE–PAR* gradients.

This simplified monotonic Michaelis–Menten model only describes saturation without photoinhibition. Thus, the mild high-light reduction in carbon uptake is a genuine field pattern revealed by bin-averaged observations, not an artifact of model fitting. This behaviour is typical of high-elevation alpine ecosystems and differs from saturation-only light responses in lowland grasslands.

2.6.2 Binned-average visualization and piecewise-linear threshold detection

To systematically resolve the synergistic regulation and stress-modifying effects of environmental factors on carbon exchange in alpine ecosystems, the bin-averaging method (Wang et al., 2017) was used to suppress random noise in field observations: according to the actual data range of each site, *PAR*, *VPD*, *SWC*, and *TS*/*TA* were grouped into gradient bins of 50 μmol·m^{-2}·s^{-1}, 120 Pa, 0.01 m^3/m^3, and 1 °C, respectively, and mean *NEE* was computed for each bin to construct *NEE*–environmental factor response curves. On this basis, piecewise linear regression was performed on the raw *NEE* observations for each response relationship, and statistically significant breakpoints were identified using F-tests; only statistically significant response thresholds were retained.

Two-segment piecewise linear regression via the pwlf package identified breakpoints of daytime ($PAR > 10$) *NEE*–environment relationships (Muggeo, 2003; Jekel and Venter, 2019). Two objective criteria validated breakpoints: ≥ 30 samples per segment, and breakpoints lying within the 20%–80% quantile of predictors; violations were marked as inadequate samples or marginal breakpoints. Bootstrap resampling (100 replicates) yielded 95% confidence intervals for breakpoints, reported as continuous uncertainty metrics without arbitrary thresholds. Data-driven breakpoint detection inflates Type I error. Therefore, the slope-change t-test was adopted as the primary criterion for breakpoint significance, while nested-model F-tests

https://doi.org/10.5194/egusphere-2026-6536
Preprint. Discussion started: 22 November 2026
© Author(s) 2026. CC BY 4.0 License.

served as supplementary statistics (Toms and Lesperance, 2003). A valid breakpoint required significance in both tests ($p < 0.05$) and compliance with the above screening criteria. Two sensitivity tests were implemented: 10%–90% quantile constraint (sen1) and no quantile constraint (sen2). All three schemes were run independently, with breakpoint uncertainty reported in Results.

2.7 Multi-model weighted comprehensive importance score

To quantify environmental controls on *NEE* variability and overcome single-model bias, we integrated four approaches — RF, Principal Component Analysis (PCA), multiple linear regression (MLR), and Pearson correlation (COR) — into a weighted composite scoring framework capturing linear, nonlinear and interactive effects. *NEE* was analysed separately for daytime ((*PAR* > 10 μmol m^{-2} s^{-1}), nighttime (*PAR* < 10 μmol m^{-2} s^{-1}) and the full day. Half-hourly records with missing *PAR* were excluded from the day/night classification, and no record fell exactly on the 10 μmol m^{-2} s^{-1} threshold.

Weights were assigned based on each model's explanatory power (Zhang et al., 2025): RF can capture nonlinear interactions and is suitable for characterizing the multi-factor co-regulatory features of alpine carbon fluxes. MLR and PCA quantify the independent linear contributions and global variance contributions of factors, respectively, offering complementary analytical dimensions. Pearson correlation describes simple linear associations. The entropy weight method was adopted to determine the weights of these methods, and the formula for the composite score is shown below:

$$Composite_{score} = 0.429F_{RF} + 0.146F_{PCA} + 0.223F_{MLR} + 0.202F_{COR} \quad (3)$$

Where $\mathrm{Composite_{score}}$ is the multi-model composite contribution score, and $\mathrm{F_{RF}}$, $\mathrm{F_{PCA}}$, $\mathrm{F_{MLR}}$ and $\mathrm{F_{COR}}$ denote the normalized factor scores from random forest, multiple linear regression, principal component analysis, and Pearson correlation analysis, respectively.

Raw scores from the four models were min–max normalized to [0,1]. Absolute values of standardized MLR coefficients and Pearson correlations were used before normalization to unify contribution assessment direction. To verify model robustness, five weighting schemes (subjective weighting, entropy weight method, CRITIC method, combined subjective-objective weighting and equal weighting) were adopted for repeated calculations. Monte Carlo simulation with 10,000 randomly sampled weight sets was further used for perturbation tests (Pianosi et al., 2016; Greco et al., 2019).

2.8 Statistical tests

Welch's two-sided t-tests (with significance thresholds at $p < 0.05$, 0.01 and 0.001) compared bin-scale *NEE* differences between sunny and cloudy conditions, accounting for unequal variances. All data processing, model fitting and statistics were implemented in Python 3.x using pvlib (0.15.2), statsmodels, scikit-learn, and scipy. Analysis of covariance (ANCOVA) with *TA* and *VPD* as covariates was further applied to test cloudy-versus-sunny *NEE* differences within the 500–750 μmol·m^{-2}·s^{-1} *PAR* bin.

This study adopts a unified technical framework: data acquisition → data processing → multi-scale analysis → mechanism interpretation. Continuous observations of CO_2 fluxes and key environmental variables (*PAR, TA, TS, SWC, VPD*) were collected from three eddy-covariance flux sites in the TRHR. Raw high-frequency data were preprocessed in EddyPro with four-dimensional quality control and gap-filling to produce comparable 30-min *NEE* time series across sites. Four analytical threads were implemented: (1) sky clearness index (*CI*) was used to separate clear and cloudy conditions; Welch's t-test was used to contrast *NEE* under sunny and cloudy conditions, while standardized anomaly analysis and the Mann–Kendall test were applied to characterize the seasonal and interannual *NEE* dynamics, respectively; (2) STL decomposition was used to extract long-term trends and seasonal oscillations of environmental drivers; (3) the Michaelis–Menten light-response model, bin-averaging method and piecewise linear regression were combined to detect nonlinear response thresholds of *NEE* to environmental factors and their confidence intervals; (4) RF, PCA, MLR and COR analysis were integrated into a multi-model weighted scoring framework to quantify dominant controls on *NEE* at daytime and full-day scales. This work systematically

https://doi.org/10.5194/egusphere-2026-6536
Preprint. Discussion started: 22 November 2026
© Author(s) 2026. CC BY 4.0 License.

reveals spatiotemporal variations and environmental mechanisms of carbon exchange in typical alpine ecosystems of the Three-River Headwaters region. The technical workflow is illustrated in Fig. 2.

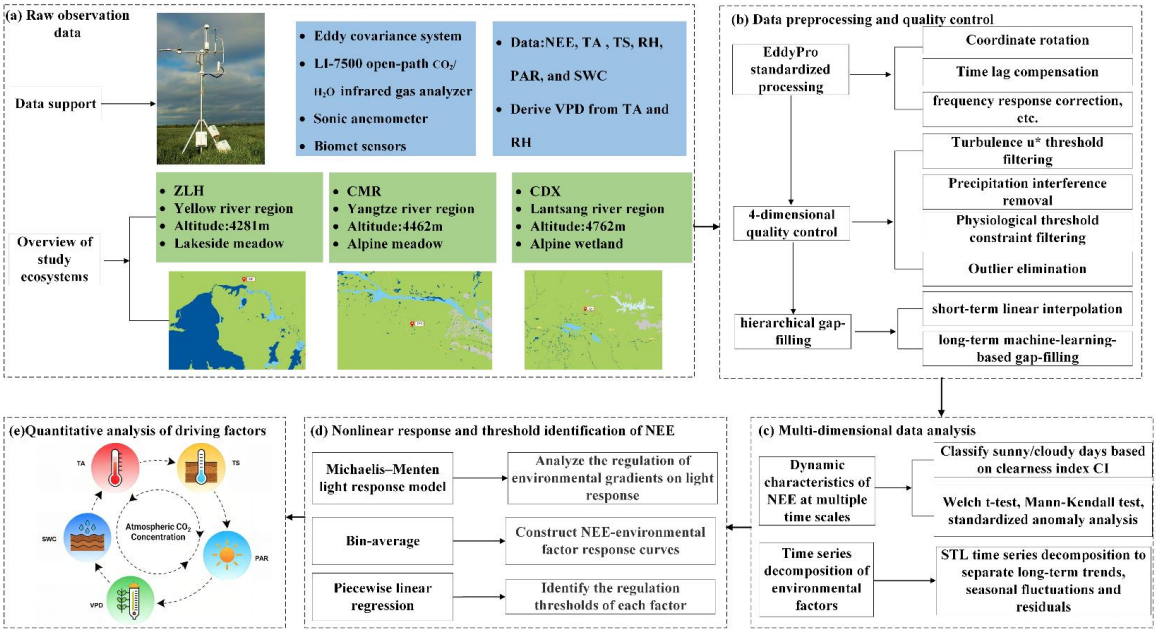


Figure 2. Technical roadmap of this study.

Notes: *PAR*, photosynthetically active radiation; *TS*, soil temperature; *SWC*, soil volumetric water content; *VPD*, vapour pressure deficit; *NEE*, net ecosystem CO_2 exchange.

3 Results

3.1 Temporal dynamics of carbon fluxes

3.1.1 Diurnal *NEE* variations under sunny and cloudy conditions

Diurnal analysis was conducted using eddy covariance observations from July–August 2023, the period of highest air temperature, peak vegetation biomass and maximum photosynthetic rates in the study area (Wu et al., 2010). Samples were classified into sunny and cloudy groups based on the clearness index (CI), and diurnal *NEE* characteristics under the two sky conditions were analysed (Fig. 3a). The diurnal *NEE* dynamics of all three ecosystems followed a single-valley U-shaped pattern: from night to early morning (approximately 20:30–08:30) *NEE* remained positive and respiratory carbon release dominated, whereas during the daytime (approximately 08:30–19:30) *NEE* turned negative and net photosynthetic uptake prevailed. Net carbon uptake deepened through the late morning and reached its diurnal minimum (trough) in the early afternoon — at about 12:30–13:00 for CDX and about 13:30–14:00 for ZLH and CMR — while respiratory release peaked in the first hours after sunset, between about 21:00 and 23:30 depending on ecosystem and sky condition. Net daily carbon sink strength followed the order CMR > ZLH > CDX.

The three ecosystems differed in the amplitude and in the day–night partitioning of their *NEE*. CMR showed the strongest daytime net uptake, with the most negative daytime mean *NEE* (−2.29 μmol $CO_2 \cdot m^{-2} \cdot s^{-1}$ on sunny and −2.93 μmol $CO_2 \cdot m^{-2} \cdot s^{-1}$ on cloudy days) and the deepest daytime trough, which was centred near 14:00 and reached −4.10 (sunny) and −4.64 (cloudy) μmol $CO_2 \cdot m^{-2} \cdot s^{-1}$. ZLH showed the smallest diurnal fluctuation (full-day amplitude about 3.8–3.9 μmol $CO_2 \cdot m^{-2} \cdot s^{-1}$), with a sunny-day trough of about −2.68 μmol $CO_2 \cdot m^{-2} \cdot s^{-1}$ (near 13:30); its daytime carbon uptake was the weakest of the three, comparable to that of CDX. CDX combined moderate daytime net uptake (daytime mean −1.45 on sunny and −1.95 μmol

https://doi.org/10.5194/egusphere-2026-6536
Preprint. Discussion started: 22 November 2026
© Author(s) 2026. CC BY 4.0 License.

$CO_2 \cdot m^{-2} \cdot s^{-1}$ on cloudy days) with by far the strongest nighttime respiration under both sky conditions (nighttime mean 1.28 on sunny and 2.21 μmol $CO_2 \cdot m^{-2} \cdot s^{-1}$ on cloudy days, versus 0.67/0.90 at CMR and 0.51/0.60 at ZLH), with nocturnal maxima of 2.42 (sunny, ~07:30) and 3.13 (cloudy, ~06:30) μmol $CO_2 \cdot m^{-2} \cdot s^{-1}$ and local peaks of 1.53/2.80 μmol $CO_2 \cdot m^{-2} \cdot s^{-1}$ during 02:00–04:00.

Comparisons between sky conditions showed that daytime *NEE* at identical midday hours (12:00–14:00) was consistently more negative (stronger carbon uptake) on cloudy days than on sunny days in all ecosystems (sunny vs cloudy: CMR −3.72 vs −4.45, ZLH −2.64 vs −2.94, CDX −2.64 vs −3.26 μmol $CO_2 \cdot m^{-2} \cdot s^{-1}$). At night, respiration was likewise higher on cloudy days, most markedly at CDX (nighttime mean 1.28 vs 2.21 μmol $CO_2 \cdot m^{-2} \cdot s^{-1}$), while the sunny–cloudy difference was smaller at CMR (0.67 vs 0.90) and ZLH (0.51 vs 0.60).

In terms of daily means, CDX remained close to carbon-neutral, acting as a weak carbon sink on sunny days and a weak carbon source on cloudy days (−0.02 vs 0.24 μmol $CO_2 \cdot m^{-2} \cdot s^{-1}$), whereas CMR and ZLH acted as clear net carbon sinks under both sky conditions (CMR −0.74 sunny vs −0.92 cloudy; ZLH −0.53 sunny vs −0.62 cloudy). Thus, although midday uptake was universally stronger on cloudy days, the daily net carbon uptake was strengthened on cloudy days at CMR and ZLH but weakened at CDX, which shifted from a weak sink to a weak source.

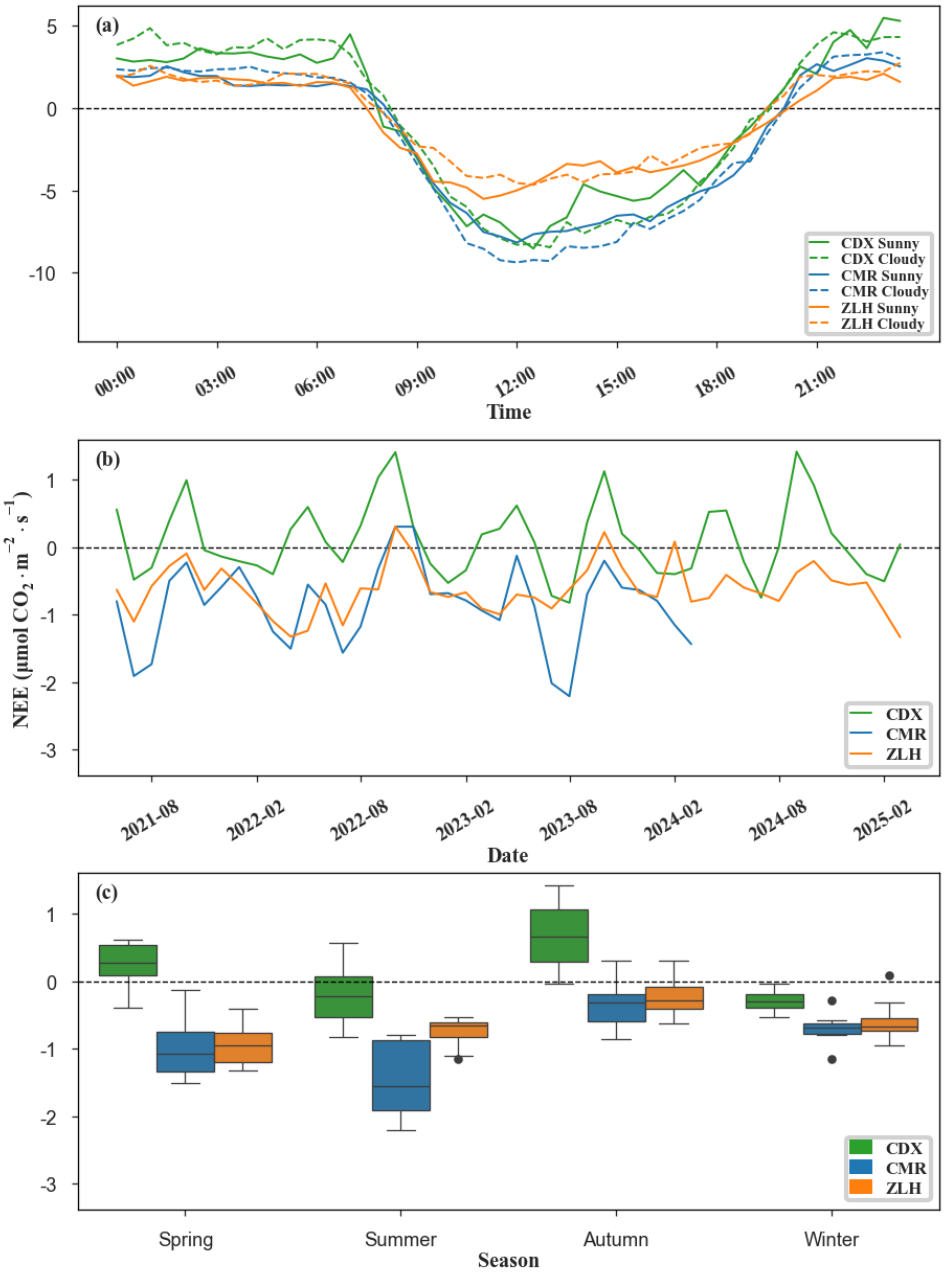
To test the statistical significance of these sunny–cloudy differences, *PAR*-binned analysis of covariance (ANCOVA, controlling for *TA* and *VPD*) revealed a significant light-intensity dependence of the diffuse-radiation promotion effect in alpine ecosystems: only within the moderate *PAR* range of 500–750 μmol·$m^{-2} \cdot s^{-1}$ was cloudy-day *NEE* significantly lower than sunny-day *NEE* across ecosystems ($p < 0.001$); no cloudy samples were available in the high-*PAR* range, and the effect was not significant in the low-light range due to limited samples.

3.1.2 Monthly and seasonal *NEE* variations

At the monthly scale (Fig. 3b), seasonal trajectories of *NEE* generally converged across ecosystems with broadly synchronized seasonal troughs, though pronounced regional differences remained. Averaged over all ecosystems, summer exhibited the strongest carbon uptake with a mean *NEE* of −0.80 μmol $CO_2 \cdot m^{-2} \cdot s^{-1}$ (strong carbon sink). Although photosynthesis nearly ceased in winter and respiration dominated the carbon exchange, low air temperatures and snow cover strongly suppressed respiratory carbon release, so the regional mean *NEE* remained weakly negative (−0.53 μmol $CO_2 \cdot m^{-2} \cdot s^{-1}$; a weak carbon sink). Spring and autumn represented transition seasons, with mean *NEE* of −0.57 and 0.05 μmol $CO_2 \cdot m^{-2} \cdot s^{-1}$, respectively. Carbon sink capacity was comparable between winter and spring, reached its annual maximum in summer, and then declined sharply; autumn was the only season with net carbon release on average and therefore showed the weakest carbon uptake of the year.

Seasonal cross-site comparison (Fig. 3c) showed that CMR exhibited the strongest carbon sink strength and acted as a significant carbon sink across all four seasons, with an especially prominent summer uptake (climatological mean of −1.83 μmol $CO_2 \cdot m^{-2} \cdot s^{-1}$ in July). It maintained a moderate carbon sink in winter (−0.71) and represented the ecosystem with the most vigorous carbon exchange (largest monthly standard deviation, 0.60); the proportion of carbon-source months was only 4.3%. ZLH was a persistent net carbon sink throughout the year with minimal variability (smallest monthly standard deviation, 0.37), showing a regular seasonal pattern and high interannual stability (carbon-source months accounted for 6.5%). CDX acted as a weak net carbon source overall with marked seasonal contrasts: weak uptake in both summer (−0.20) and winter (−0.29) but net carbon release in spring (0.24) and autumn (0.70); 52.2% of months acted as carbon sources, indicating obvious seasonal shifts in sink function. Uniquely at this site, winter uptake slightly exceeded summer uptake, deviating from the regional summer-maximum pattern. Because CDX was the only site that turned into a source in autumn, the regional autumn mean also became a net release, whereas CMR and ZLH remained net sinks throughout the year.

https://doi.org/10.5194/egusphere-2026-6536
Preprint. Discussion started: 22 November 2026
© Author(s) 2026. CC BY 4.0 License.



310

Figure 3. Diurnal, monthly, and seasonal variations in *NEE* across the three ecosystems: (a) diurnal variation in *NEE*; (b) monthly variation in *NEE*; and (c) seasonal variation in *NEE*. CMR observations ended in April 2024; therefore, no 2025 CMR data are shown in the figure.

3.1.3 Interannual *NEE* dynamics, cumulative fluxes, and anomalies

315 In terms of interannual variation (Fig. 4a), annual *NEE* for all three alpine ecosystems followed fluctuating U-shaped or near-U-shaped annual trajectories, with marked spatial differences in amplitude, peak magnitude and sink strength. Multi-year mean *NEE* ranked CMR (−0.85 μmol $CO_2 \cdot m^{-2} \cdot s^{-1}$) < ZLH (−0.59) < CDX (0.11): CMR and ZLH were persistent carbon sinks, whereas CDX (0.11) acted as a net source throughout. Annual means ranged −0.896 to −0.693 (CMR; two complete years),

https://doi.org/10.5194/egusphere-2026-6536
Preprint. Discussion started: 22 November 2026
© Author(s) 2026. CC BY 4.0 License.

−0.689 to −0.491 (ZLH; three complete years), 0.037 to 0.233 (CDX; three complete years). Recomputing multi-year means over the common window (June 2021–March 2024) reproduced the same ranking, indicating the contrast is not an artefact of record length.

Mann–Kendall tests on annual mean *NEE* combined with Sen's slope estimator showed clear spatial heterogeneity in trend strength, with no site displaying a statistically significant monotonic trend. Sen's slopes (μmol CO_2 m^{-2} s^{-1} yr^{-1}) were −0.130 at CMR (4 valid observations), −0.030 at ZLH (5 valid observations) and −0.087 at CDX (5 valid observations), with 95% confidence intervals of −0.214 to 0.247, −0.245 to 0.115 and −0.470 to 0.093, respectively; all intervals included zero. Exact two-sided p-values were 0.750, 0.817 and 0.233. With only four annual values the smallest attainable two-sided p-value is 0.083, so the test has essentially no power to detect a trend at CMR, and the absence of significance therefore does not imply the absence of a trend. Because the records span less than four years (2.8–3.8 years), these slopes describe stage-specific variability only and should not be extrapolated to long-term climatic responses.

Cumulative *NEE* complemented the trend results (Fig. 4b). CMR had the largest uptake (−910.9 g C m^{-2}), sustaining high net sequestration throughout its record (ending April 2024). ZLH ranked second (−837.7 g C m^{-2}), consistent with its stable annual mean sink strength. By contrast, CDX was a net source (cumulative 153.2 g C m^{-2}). The ranking was unchanged over the common window, and the contrast is not attributable to unequal record length, because the site with the shortest record (CMR) still showed the largest cumulative uptake (CMR 1031 d; ZLH 1370 d; CDX 1386 d).

Cumulative anomalies (relative to the multi-year mean) revealed broadly synchronized turning points and fluctuation cycles (Fig. 4c), indicating coherent regional climatic forcing, while local controls created differing departure magnitudes. CMR had the broadest range (−64.2 to 67.2; range 131.4 g C m^{-2}) with intense oscillations and frequent sink–source shifts, the most variable site. CDX ranked second (108.2), whereas ZLH had the narrowest range (−72.7 to 22.8; range 95.5 g C m^{-2}), with mild oscillations and the most stable response.

Standardized anomalies (±2 SD relative to the daily calendar-month climatology) were distributed throughout the year rather than confined to mid-summer. The monthly climatology differed markedly: the deepest sinks occurred in July for CMR and in April for ZLH, while CDX was weakest and peaked as a source in October (1.12 μmol $CO_2 \cdot m^{-2} \cdot s^{-1}$). Positive, source-strengthening anomalies dominated at CDX (63/9 of 72 events) and ZLH (48/15 of 63), and were nearly balanced at CMR (22/20 of 42). CMR showed repeated late-summer sink-strengthening anomalies in each of three years. These short pulses did not shift long-term trends but underscore the strong modulation of alpine carbon budgets by extreme summer hydrothermal variability.

https://doi.org/10.5194/egusphere-2026-6536
Preprint. Discussion started: 22 November 2026
© Author(s) 2026. CC BY 4.0 License.

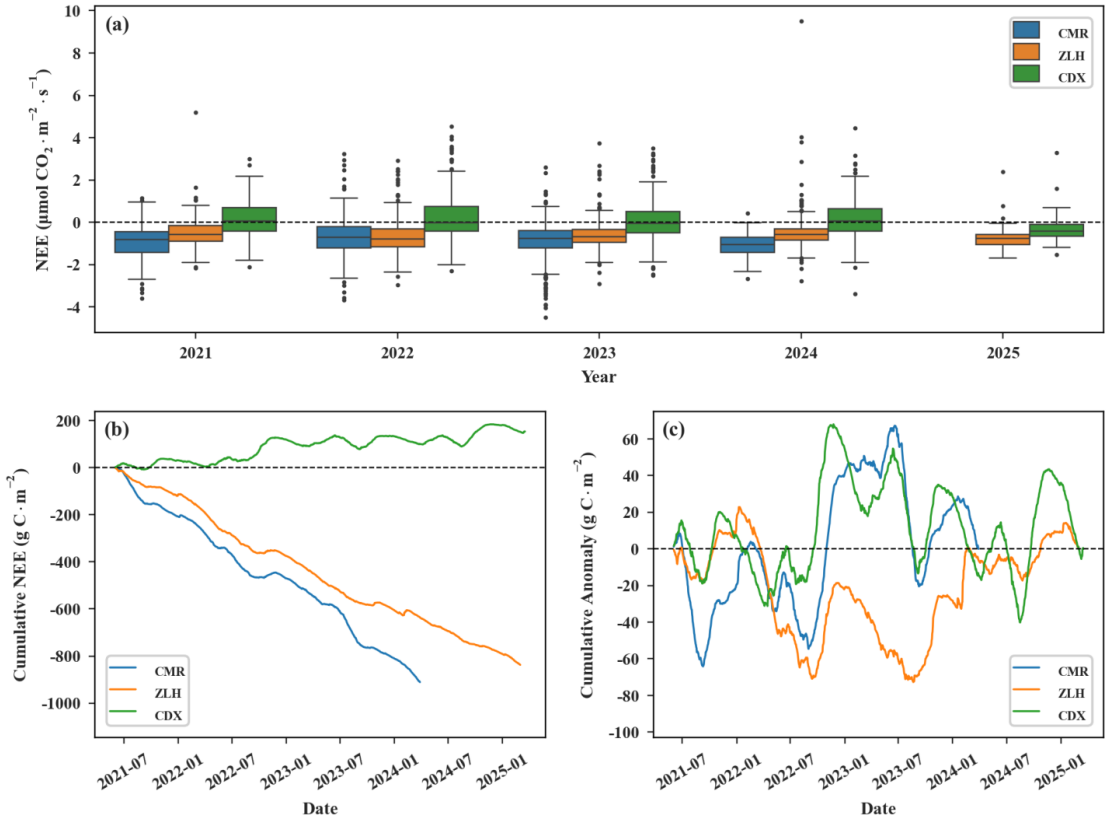


Figure 4. Interannual variation of *NEE* across the three ecosystems: (a) Boxplots of half-hourly *NEE* (μmol $CO_2 \cdot m^{-2} \cdot s^{-1}$) for each year. (b) Time series of cumulative *NEE* (g $C \cdot m^{-2}$) at CMR, ZLH and CDX. (c) Cumulative *NEE* anomalies (g $C \cdot m^{-2}$). CMR observations ended in April 2024, so 2025 data of CMR are absent in figure.

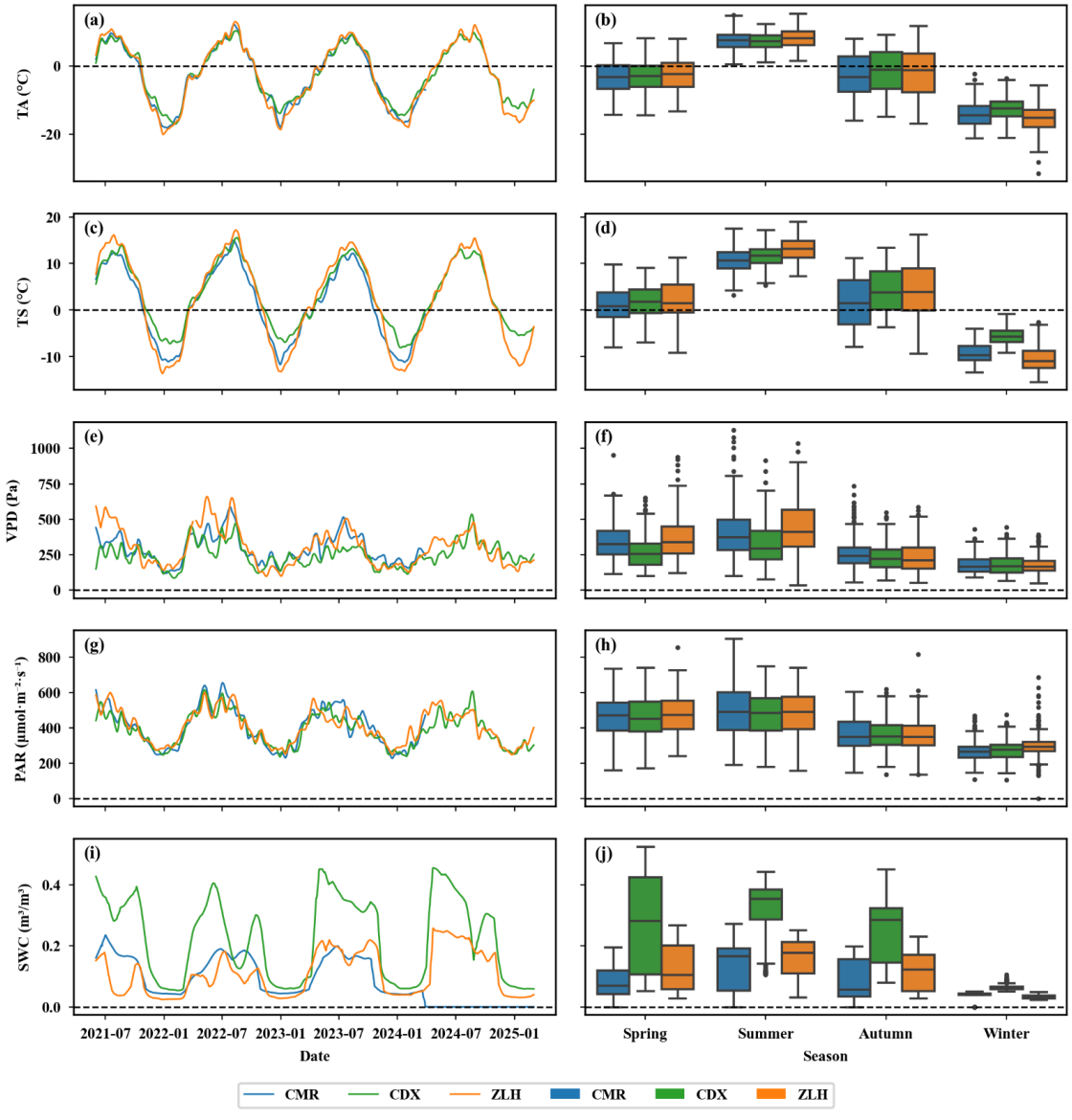
3.2 Environmental controls on carbon fluxes

3.2.1 Temporal dynamics of climatic factors

Time-series analysis of five climatic factors (*TA*, *PAR*, *SWC*, *VPD*, *TS*) was conducted using Seasonal and Trend decomposition using Loess (STL) decomposition. The STL decomposition (Figs. 5a–j, Table 1) revealed pronounced spatial heterogeneity in multi-year mean values for all five variables. Most drivers showed highly significant trends ($p < 0.0001$), but trend directions and magnitudes diverged among ecosystems. *PAR* and *TS* decreased consistently at all ecosystems; the decline rate of *PAR* at CDX was markedly higher than at CMR and ZLH. *VPD* showed mixed increasing–decreasing patterns with the most prominent regional divergence, where ZLH experienced the largest decreasing magnitude. *TA* and *SWC* displayed binary divergence: decreasing only at CMR while increasing synchronously at CDX and ZLH. Model explanatory power showed polarized performance: The relationships of *TA*, *TS* and *SWC* with *NEE* had high R^2 values ranging from 0.75 to 0.91; *PAR* exhibited a moderate relationship (R^2 of 0.72), and the relationship for *VPD* was negligible (R^2 of 0.02); *VPD* exhibited large discrepancies among ecosystems, with $R^2 > 0.9$ at ZLH, but below 0.02 at CMR and CDX; *PAR* showed moderate explanatory power with minor inter-site differences. In terms of seasonal fluctuation (peak-to-trough amplitude), all five variables presented consistent and stable periodic cycles. *VPD* and *PAR* possessed the largest absolute amplitudes, whereas *TA*, *TS* and *SWC* had relatively low absolute amplitudes (all below 50) with evident seasonal variation. *SWC* followed a U-shaped pattern with higher values in winter-spring and lower values in summer-autumn. STL residuals were dominated by stochastic

https://doi.org/10.5194/egusphere-2026-6536
Preprint. Discussion started: 22 November 2026
© Author(s) 2026. CC BY 4.0 License.

fluctuations without detectable long-term trends or periodicity, indicating effective separation of trend and seasonal components.



370 **Figure 5. Inter-annual temporal variations and seasonal distribution characteristics of environmental factors in different ecosystems (a, c, e, g, i) Inter-annual variation lines of *TA*, *TS*, *VPD*, *PAR* and *SWC*, respectively; (b, d, f, h, j) Corresponding seasonal box whisker plots for each factor.**

Table 1 Summary of interannual trends and seasonal characteristics of environmental factors based on STL time-series decomposition

Factor	Multi-year mean ranging	Value range	Trend (slope R^2)	Trend direction	Seasonal amplitude	Seasonality
TA	CDX(-2.29)>ZLH>CMR(-2.99)	-28–15°C	(-0.0005, 0.75)	Non-uniform	34.67	Marked
TS	CDX(2.34)>ZLH>CMR(1.15)	-15–18°C	(-0.0017, 0.98)	Uniform	27.03	Marked

https://doi.org/10.5194/egusphere-2026-6536
Preprint. Discussion started: 22 November 2026
© Author(s) 2026. CC BY 4.0 License.

VPD	ZLH(304.56)>CMR>CDX(254.11)	33–1190 Pa;	(-0.0160, 0.02)	Non-uniform	1011.10	Pronounced
PAR	ZLH(401.19)>CMR>CDX(390.76)	100–850 μmol·m^{-2}·s^{-1}	(-0.0117, 0.72)	Uniform	770.49	Pronounced
SWC	CDX(0.23)>CMR>ZLH(0.11)	0.02–0.50 m^3/m^3	(-0.0009, 0.91)	Non-uniform	0.23	Marked

Notes: Values in parentheses under ranking of multi-year mean values are multi-year means of the corresponding factor at each site, sharing identical units with the same factor in value range (raw);In trend (slope yr^{-1}, R^2), A negative slope indicates a significant decreasing trend, whereas a positive slope denotes a significant increasing trend; STL: Seasonal and Trend decomposition using Loess.

3.2.2 Controls of environmental factors on carbon fluxes

Considering the distinct regulatory mechanisms of climatic factors on *NEE* between growing and non-growing seasons, valid daytime flux data from the growing season were selected in this study to systematically explore the light-response patterns, environmental modulation effects and non-linear threshold characteristics of *NEE* in alpine ecosystems. Fitting results of the *PAR*-*NEE* light-response based on the Michaelis-Menten model (Fig. 6a) showed that *NEE* exhibited an increase-then-decrease trend with rising *PAR* across all ecosystems during the growing season. Carbon uptake continuously increased with light intensity below the threshold, while photoinhibition induced a slight decline in carbon uptake beyond the threshold. Negative *NEE* values denote net ecosystem carbon uptake, and absolute values are adopted for subsequent parameter comparisons (Zhao et al., 2006). For the light response parameters, the apparent quantum efficiency α followed the order of CMR(0.0072)>CDX(0.0057)>ZLH(0.0049). CMR exhibited the highest α value, indicating the strongest sensitivity to *PAR* variations, while ZLH showed the weakest sensitivity. For maximum photosynthetic rate (F_{max}), the sequence was CMR(10.43)>CDX(9.85)>ZLH (6.87). CMR had the strongest carbon sequestration potential, whereas ZLH possessed the weakest carbon sequestration potential.

The *NEE*–*PAR* responses across *VPD* gradients (Figs. 6b–d) showed progressive weakening with rising atmospheric water stress: marked *NEE* decline with *PAR* and distinct inter-ecosystem curve divergence at low *VPD*, partially attenuated *PAR* control and converging curves at moderate *VPD*, and greatly suppressed *PAR* effects with weak negative *NEE*–*PAR* correlation at high *VPD* where carbon exchange was dominated by water availability. *NEE*–*PAR* responses along *TA* gradients (Figs. 6e–g) indicated inhibited photosynthesis at low air temperature with slow *NEE* decline under rising *PAR* and large inter-ecosystem differences; moderate air temperature alleviated thermal limitation and improved photosynthetic efficiency to strengthen responses and curve convergence, while high temperature weakened responses again with weak negative correlation, implying high-temperature stress triggered midday depression, elevated respiration or aggravated water stress. *TS* gradients exhibited similar *NEE*–*PAR* patterns to *TA* (Figs. 6h–j): low soil temperature suppressed microbial and root activity, causing slow *NEE* decline and pronounced cross-ecosystem divergence; responses strengthened and curves converged at moderate soil temperature but weakened under high soil temperature, when carbon exchange was governed by non-photonic factors including water and nutrients. *NEE*–*PAR* responses across *SWC* gradients (Figs. 6k–m) revealed water limitation prevailed at low *SWC*, inducing rapid *NEE* decline with *PAR* and clear inter-ecosystem divergence (Gu et al., 2003); responses weakened and curves converged at moderate *SWC*, and *PAR* regulation was further diminished at high *SWC* with only weak negative *NEE*–*PAR* correlation. The derived *NEE* response thresholds for each environmental factor are summarized in Table 2.

https://doi.org/10.5194/egusphere-2026-6536
Preprint. Discussion started: 22 November 2026
© Author(s) 2026. CC BY 4.0 License.

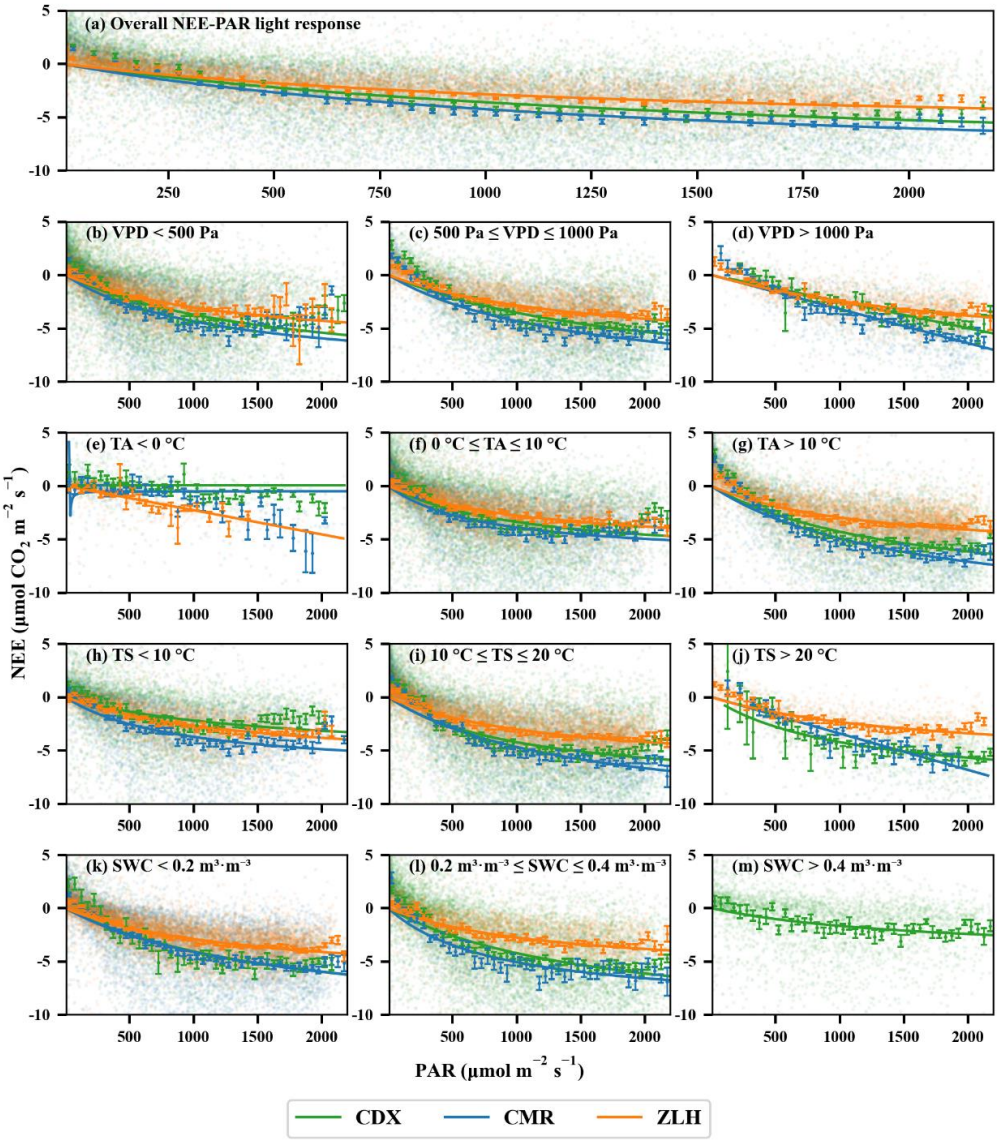
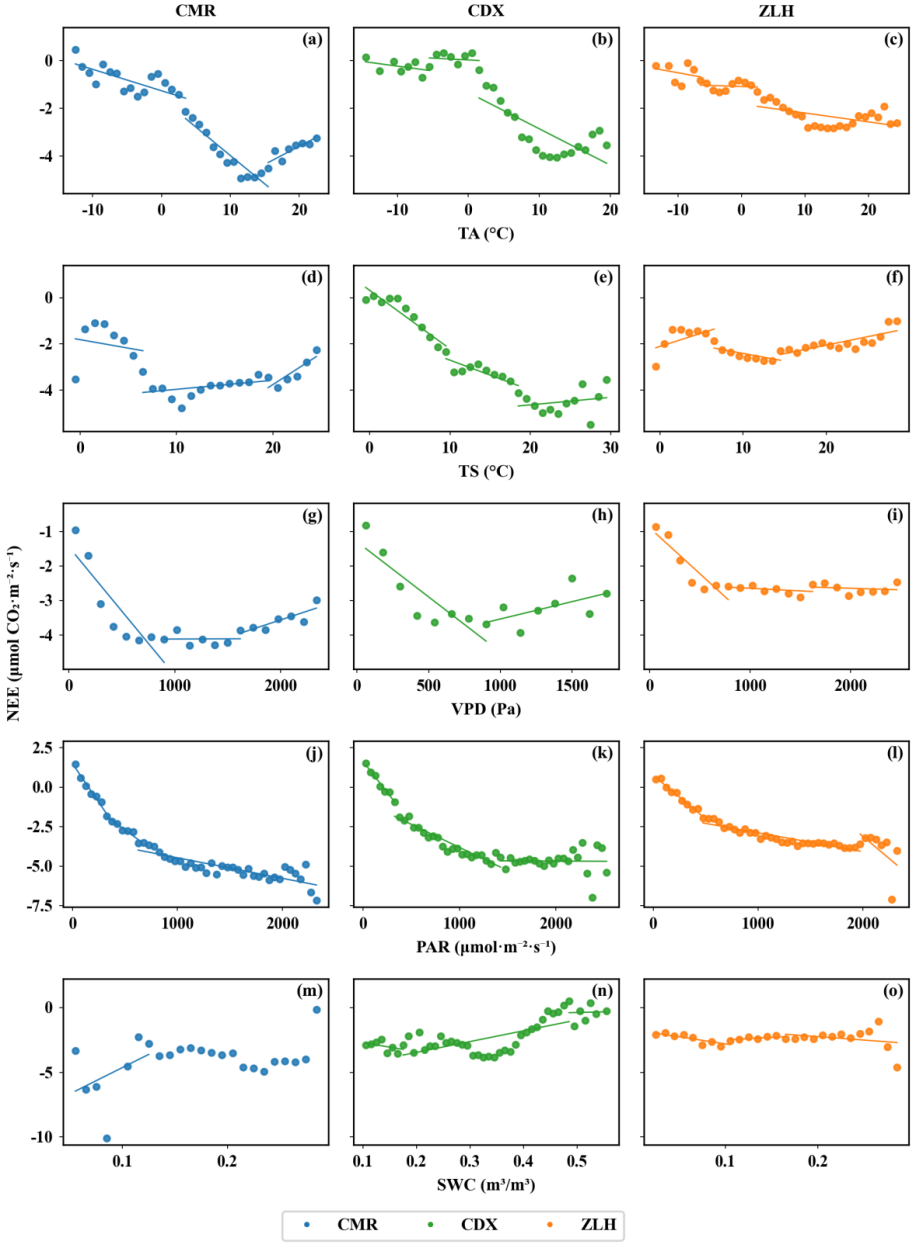


Figure 6. Michaelis–Menten light response fits of *NEE* vs. *PAR* for each ecosystem under overall conditions and across different environmental factor gradients: (a) overall *NEE–PAR* light response; (b) *VPD* < 500 Pa; (c) 500 Pa ≤ *VPD* ≤ 1000 Pa; (d) *VPD* > 1000 Pa; (e) *TA* < 0 °C; (f) 0 °C ≤ *TA* ≤ 10 °C; (g) *TA* > 10 °C; (h) *TS* < 10 °C; (i) 10 °C ≤ *TS* ≤ 20 °C; (j) *TS* > 20 °C; (k) *SWC* < 0.2 m³ m⁻³; (l) 0.2 m³ m⁻³ ≤ *SWC* ≤ 0.4 m³ m⁻³; and (m) *SWC* > 0.4 m³ m⁻³. Note that *SWC* > 0.4 m³ m⁻³ occurs only at CDX; CMR and ZLH never reach this soil moisture threshold.
Notes: scattered points denote the raw daytime half-hourly flux observations.

Results of single-factor responses derived from Bin-average binning (Fig. 7) reveal pronounced non-linear relationships between each environmental factor and daytime *NEE*. *TA* exhibited a rise-then-fall nonlinear pattern with *NEE* (Figs. 7a–c): moderate warming promoted carbon sink, while further warming reduced carbon uptake, and high-temperature stress suppressed photosynthesis beyond the threshold (Geng and Xu, 2017). *TS* also displayed a rise-then-fall nonlinear relationship with *NEE* (Figs. 7d–f): optimum soil temperature facilitated carbon uptake, whereas values outside this range induced inhibition; soil warming under frozen conditions increased microbial substrate supply and soil carbon emission (Liang and Zhu, 2021; Weng et al., 2022). *VPD–NEE* responses (Figs. 7g–i) indicated that daytime ecosystem carbon uptake rose with

https://doi.org/10.5194/egusphere-2026-6536
Preprint. Discussion started: 22 November 2026
© Author(s) 2026. CC BY 4.0 License.

increasing *VPD* before declining after crossing a threshold; optimal *VPD* boosted ecosystem CO_2 assimilation, while excessive *VPD* aggravated atmospheric drought stress, triggering stomatal closure and suppressing carbon uptake. The *PAR*–*NEE* relationship was nonlinear with an initial increase followed by a decrease (Figs. 7j–l): *PAR* dominated carbon assimilation under low light and enhanced carbon uptake, and beyond the light-saturation threshold, photoinhibition, midday depression and elevated respiration slightly reduced carbon uptake. *SWC* showed marked nonlinearity with *NEE* (Figs. 7m–o): moderate *SWC* sustained strong carbon sink; low *SWC* induced stomatal closure and inhibited carbon uptake (Reichstein et al., 2002), while excessive *SWC* caused soil hypoxia, restraining root and microbial activity and weakening carbon sequestration (Sun et al., 2021).



https://doi.org/10.5194/egusphere-2026-6536
Preprint. Discussion started: 22 November 2026
© Author(s) 2026. CC BY 4.0 License.

Figure 7. Binned average response relationships between *NEE* and *TA*, *TS*, *VPD*, *PAR*, and *SWC* for each ecosystem: (a–c) binned responses of *NEE* to *TA* for the CMR, CDX, and ZLH ecosystems, respectively; (d–f) binned responses of *NEE* to *TS* for the CMR, CDX, and ZLH ecosystems, respectively; (g–i) binned responses of *NEE* to *VPD* for the CMR, CDX, and ZLH ecosystems, respectively; (j–l) binned responses of *NEE* to *PAR* for the CMR, CDX, and ZLH ecosystems, respectively; and (m–o) binned responses of *NEE* to *SWC* for the CMR, CDX, and ZLH ecosystems, respectively.

Notes: this figure is only intended to visually illustrate response trends. The breakpoint thresholds were calculated from the raw half-hourly flux data rather than extracted from the binned average outputs.

Overall, CDX was most sensitive to hydrothermal stress with the largest response magnitude (exhibiting the strongest enhancement or suppression effects for *VPD, TA* and *TS*), CMR remained the most stable across all factor gradients with the highest adaptability (weakest regulation by all environmental factors), and ZLH was intermediate; all ecosystems showed typical gradient response patterns with clear divergence.

Piecewise linear regression was performed on raw hourly observations, with three quantile constraint schemes (main, sen1, sen2) adopted for sensitivity analysis. The results showed that breakpoints for all 15 site-factor combinations were significant under sen1 and sen2 schemes; 14 out of 15 combinations remained significant under the main scheme, while the remaining one (CMR-*TA*) was labelled “edge breakpoint” as its breakpoint approached the lower bound of factor distribution. Most combinations (14/15) yielded consistent judgements across the three schemes, demonstrating overall result robustness; only a few breakpoints at the low end of factor distribution were sensitive to the lower quantile limit. Therefore, outputs from the main scheme (20%–80% constraints) were adopted as the primary basis for interpretation.

The results revealed distinct threshold differentiation in the regulation of *NEE* by each environmental factor (Table 2, Table A3, Table A4): 14 breakpoints across all ecosystem-factor combinations were statistically significant. Significant light saturation points of *PAR* were detected for all three ecosystems, ranging from 683.50 to 803.73 μmol·m^{-2}·s^{-1}; *NEE* uptake rates decreased markedly beyond these thresholds, showing typical light-saturation responses. Significant *VPD* thresholds (391.99–440.92 Pa) were identified in all three ecosystems, above which the inhibitory effect of *VPD* on *NEE* levelled off with slopes approaching zero. Significant breakpoints were found for *TS* (9.61–11.45°C) and *SWC* (0.08–0.35 m^3/m^3) across the three ecosystems. Significant *TA* breakpoints (10.67–12.87 °C, located at the lower end of the factor range) were detected in two ecosystems, whereas CMR failed the main quantile constraint and was classified as an “edge breakpoint”, excluded from the statistics of significant breakpoints in the primary results. Nevertheless, sensitivity tests using sen1 and sen2 schemes confirmed its statistical significance, suggesting that the regulation of CMR *NEE* by *TA* likely follows a threshold-type response, with the threshold close to the lower limit of observed values.

Table 2 Fitting parameters of piecewise regression breakpoints between net ecosystem exchange and environmental factors

Ecosystem	Factor	Unit	n	Breakpoint (main)	95% CI (main)	Sig. (main)	Slope$_1$ (main)	Slope$_2$ (main)	R^2 (main)	Consistent
CDX	*SWC*	m^3/m^3	14351	0.3539	[0.348, 0.363]	*	-4.0275	31.3069	0.0527	Y
	PAR	μmol·m^{-2}·s^{-1}	14351	803.727	[685.619,871.580]	*	-0.0066	-0.0006	0.2419	Y
	TA	°C	14297	10.667	[9.873, 11.859]	*	-0.3629	0.08	0.0975	Y
	TS	°C	14336	10.3576	[9.735, 10.759]	*	-0.3246	-0.1472	0.0827	Y
	VPD	Pa	14194	403.84	[371.591,447.820]	*	-0.0087	0.0001	0.0638	Y
CMR	*SWC*	m^3/m^3	9874	0.164	[0.163, 0.191]	*	4.7699	-19.4174	0.0096	Y
	PAR	μmol·m^{-2}·s^{-1}	9995	683.503	[544.956,855.522]	*	-0.0074	-0.0013	0.3494	Y
	TA	°C	9947	12.602	[11.451,13.240]	NS	-0.3054	0.2026	0.1189	N
	TS	°C	9995	9.61	[9.361, 10.102]	*	-0.401	0.1003	0.0729	Y

https://doi.org/10.5194/egusphere-2026-6536
Preprint. Discussion started: 22 November 2026
© Author(s) 2026. CC BY 4.0 License.

ZLH	*VPD*	Pa	9785	391.9855	[365.132,465.366]	*	-0.0095	-0.0003	0.0725	Y
	SWC	m^3/m^3	13907	0.0802	[0.076, 0.090]	*	-13.209	2.6038	0.0047	Y
	PAR	$\mu mol \cdot m^{-2} \cdot s^{-1}$	13907	714.7759	[656.999,787.845]	*	-0.0047	-0.0008	0.4217	Y
	TA	°C	13849	12.8723	[11.720,14.012]	*	-0.1415	0.0748	0.0663	Y
	TS	°C	13907	11.448	[10.750,12.423]	*	-0.1351	0.0713	0.0263	Y
	VPD	Pa	13553	440.92	[409.563,476.527]	*	-0.005	-0.0002	0.075	Y

Notes: main: breakpoint constrained to the 20th–80th quantiles. NS: "edge breakpoint" refers to breakpoints located at the edge of factor distribution, with adequate sample size for segmented groups. "Consistent" denotes identical significance judgements among the three schemes.

3.2.3 Relative importance evaluation and uncertainty test of climatic drivers

To verify the robustness of composite scores against different weighting schemes, five weighting methods, including subjective weighting, entropy weight method, CRITIC method, combined weighting, and equal weighting, were adopted for repeated calculations. A Monte Carlo perturbation test with 10,000 random weight sets was further conducted for auxiliary verification. The results showed that the primary driving factors remained consistent across all weighting schemes for all nine of the nine site-period combinations (9/9); no inconsistency was observed for any site-period under any weighting method. Additionally, the Spearman rank correlation coefficients of composite scores among the five schemes were all greater than or equal to 0.981, and the average winning probability of the primary factors reached 90.9% (see Table A5, TableA6, Table A7, Table A8 for details). These findings indicate that the ranking of factor importance is insensitive to weight selection, demonstrating the robustness and reliability of the research conclusions.

Based on daytime observational data (Fig. 8a), the integrated results from the four analytical methods indicated that daytime *NEE* variations in all three alpine ecosystems were predominantly governed by photosynthetic carbon uptake. *PAR* served as the primary driving factor at all ecosystems, with composite scores ranging between 0.85 and 0.88. However, distinct spatial heterogeneity was observed in secondary driving factors. Specifically, CMR was dominated by *TA* (0.48) as the secondary factor, followed by *VPD* (0.30), representing a "temperature–moisture co-driven" pattern. CDX exhibited the strongest *TA* contribution among the three ecosystems (0.38), with *VPD* (0.27) and *TS* (0.18) contributing in succession, reflecting multi-factor synergy. At ZLH, all non-*PAR* factor scores were ≤ 0.30 (*VPD* 0.30, *TA* 0.26, *TS* 0.17, *SWC* 0.12), indicating a predominantly radiation-driven regime. Additionally, *SWC* yielded the lowest composite scores (0.12–0.15) across all ecosystems during daytime periods, suggesting that carbon assimilation of alpine ecosystems in the growing season is primarily controlled by energy availability rather than soil moisture conditions.

Based on all-day observations (Fig. 8b), *PAR* remained the primary driver of *NEE* across all three ecosystems, with composite scores of 0.91 (CDX), 0.87 (CMR) and 0.95 (ZLH); the all-day *PAR* scores were slightly higher than the corresponding daytime values at all three ecosystems (0.05, 0.02 and 0.07, respectively). ZLH showed the highest *PAR* score (0.95) and the largest increase from daytime (0.07), with *VPD* as the only secondary factor above 0.30 (0.33). CMR showed the lowest all-day *PAR* score (0.87), slightly above its daytime value of 0.85. At CDX, *PAR* rose to 0.91 from its daytime value of 0.86, with *VPD* (0.31) as the clear secondary factor; the non-*PAR* factors (*VPD*, *SWC*, *TS*, *TA*) were closely spaced between 0.14 and 0.31, giving CDX the most balanced all-day driver structure and reflecting divergent day–night regulatory mechanisms. CMR was moderately balanced, while at ZLH the gap between *PAR* (0.95) and *VPD* (0.33) was the largest. Soil temperature (*TS*) contributions increased slightly relative to daytime, whereas *TA* contributions decreased markedly at all three ecosystems; *SWC* contributions remained low overall (0.13–0.15).

Nighttime observations (Fig. 8c) showed that photosynthesis had ceased and that the regulation of *NEE* shifted fundamentally: temperature replaced *PAR* as the dominant control, with Q_{10}-type temperature responses, and the strength of this temperature

https://doi.org/10.5194/egusphere-2026-6536
Preprint. Discussion started: 22 November 2026
© Author(s) 2026. CC BY 4.0 License.

control and the role of secondary moisture factors differed among the three ecosystems. At CDX *NEE* was dominated by *TS* (composite score 0.94), with *SWC* as the secondary contributor (0.40), indicating coupled soil hydrothermal regulation. At CMR the control by *TS* was the strongest (0.96), followed by *TA* (0.52), while the moisture influence was comparatively weak. At ZLH the temperature control was the weakest of the three ecosystems (*TS*; 0.93), and the contributions of *VPD* (0.33) and *SWC* (0.40) were the most pronounced, reflecting synergistic temperature–moisture regulation. Because *TS* and *TA* are closely coupled at night, the two are treated as a single temperature control rather than ranked against each other; *TS* ranked highest in the composite scores at all three ecosystems. Overall, *SWC* contributed much more at night than during the day (nighttime: 0.40/0.42/0.40 vs daytime: 0.13/0.12/0.15), strongly modulating nocturnal carbon release, whereas *VPD* contributions were generally lower at night (0.16/0.25/0.33 vs 0.29/0.28/0.33) and did not show a consistent increase.

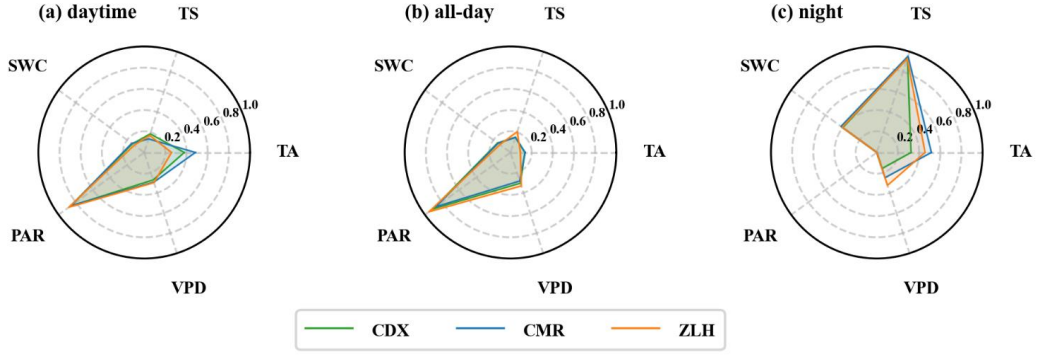


Figure 8. Influence weights of environmental factors on *NEE* for the different ecosystems: (a) comprehensive influence weights of environmental factors for daytime *NEE*; (b) comprehensive influence weights of environmental factors for all-day *NEE*; and (c) comprehensive influence weights of environmental factors for night *NEE*.

In summary, *PAR* acted as the leading driver for daytime and all-day *NEE* consistently across all ecosystems, independent of any single model, while *SWC* had the weakest explanatory power across all ecosystems. All ecosystems followed a day-*PAR* / night-temperature switching mechanism for *NEE* regulation. *SWC* exhibited time dependence: low during daytime and influential at night. The all-day pattern represented an intermediate state integrating diurnal and nocturnal processes, forming the fundamental framework controlling alpine carbon fluxes. CDX was a balanced multi-factor type with coupled soil hydrothermal processes and high sensitivity to soil variations. CMR was temperature-controlled, dominated by soil temperature at night, and most sensitive to temperature change. ZLH was radiation-limited during the daytime and all-day, and sensitive to cloud cover. This ecosystems-level differentiation persisted across all three periods and underpinned the spatial divergence of carbon sink functions among the three ecosystems.

4 Discussion

4.1 Shared temporal rhythms and differences in *NEE* among the three typical ecosystems

This study reveals multi-scale diurnal, seasonal and interannual variability in TRHR alpine *NEE*. The ecosystems follow typical alpine carbon-cycle rhythms (Chai et al., 2018; Zhang et al., 2024), yet local microclimate and threshold effects drive distinct fluctuations (Wang et al., 2021). Summer's favorable hydrothermal conditions and peak vegetation phenology boost photosynthetic uptake, making summer the primary regional carbon sink, while enhanced diffuse radiation under cloud cover further modulates midday carbon uptake. Winter photosynthesis nearly ceases, and respiratory processes dominate carbon exchange; however, low air temperatures and snow cover strongly suppress respiratory release, so the region remains a weak carbon sink overall. Spring and autumn represent source–sink transitions.

https://doi.org/10.5194/egusphere-2026-6536
Preprint. Discussion started: 22 November 2026
© Author(s) 2026. CC BY 4.0 License.

Divergent habitats and environmental thresholds drive *NEE* spatiotemporal differences. Cold, dry, highly variable CMR supports vegetation adapted to low temperature and drought, showing the strongest carbon sink yet the largest variability (cumulative-anomaly range of 131.4 g C m^{-2}), consistent with its highest daytime temperature sensitivity and nighttime air-temperature-dominated respiration. CMR also showed repeated late-summer sink-strengthening anomalies in three consecutive years. ZLH showed minimal variability and stable carbon budgets, acting as a persistent carbon-sink anchor, consistent with its purely radiation-limited driving regime and high sensitivity to cloud cover and diffuse radiation. Cold, humid CDX features coupled soil hydrothermal regulation, functioning as a weak net carbon source with strong seasonal shifts: carbon-source months accounting for 52.2% and source-strengthening positive anomalies dominated, indicating high sensitivity to soil hydrothermal variations. Synchronous turning points of cumulative anomalies across all ecosystems indicate that large-scale climate oscillations can override local habitat-driven carbon-cycle divergence and impose basin-wide controls. It should be emphasized that the detected *NEE* differences mainly arise from site-specific microclimate, hydrothermal distribution and environmental thresholds, rather than inherent ecosystem-type traits. Cross-site carbon-cycle divergence reflects vegetation adaptation to local habitat stress and stability. These findings offer site-scale evidence for spatial heterogeneity and multi-factor controls of the alpine carbon cycle.

4.2 Carbon exchange differences between sunny and cloudy conditions

The three alpine ecosystems exhibited significantly lower *NEE* under cloudy than sunny conditions at equivalent *PAR* only within the moderate photosynthetically active radiation range of 500–750 $\mu mol \cdot m^{-2} \cdot s^{-1}$, confirming the positive promotional effect of diffuse radiation on photosynthesis in high-elevation regions (Chu et al., 2015; Ren et al., 2017; Chen et al., 2018). The synergistic environmental mechanism can be preliminarily explained as follows: strong direct radiation on sunny days readily induces leaf photoinhibition and reduces light-use efficiency, while the hot, clear environment creates high *VPD*, which—on the one hand promotes stomatal closure, restricts intercellular CO_2 supply, and suppresses gross primary production (Novick et al., 2016), and—on the other hand raises plant and soil respiration rates and aggravates carbon losses (Xu et al., 2022). In contrast, on cloudy days, diffuse radiation penetrates the canopy uniformly, alleviates photoinhibition, and improves canopy light-use efficiency, while the combination of low temperature, and low *VPD* significantly suppresses ecosystem respiration and reduces carbon emissions.

This pattern in the moderate *PAR* bin was consistent across the three ecosystems, showing good local generality for TRHR alpine meadows and wetlands. Similar behaviour reported at other plateau flux sites suggests it may represent a general feature of Tibetan Plateau alpine ecosystems. However, the diffuse-radiation benefit has clear bounds: it persists under low-to-moderate light and weakens markedly at high *PAR*. Regional hydrothermal heterogeneity further modulates sunny/cloudy *NEE* controls; light is not the sole driver, and superimposed hydrothermal stress creates spatial variation in dominant regulators.

It should be noted that, constrained by observational conditions, this study did not conduct separate measurements of direct and diffuse radiation. Comparisons based on sky-type grouping alone cannot precisely isolate the independent contributions of *PAR*, *TA*, *TS*, *VPD* and *SWC*, and only the apparent characteristics of multi-factor synergistic regulation can be identified; the conditions for rigorous mechanistic attribution are therefore not yet met. Accordingly, this study only objectively describes the observed patterns of sunny–cloudy *NEE* differences and their potential synergistic pathways, and the findings should not be directly generalized as universal mechanistic conclusions. Regional carbon-sink simulations are still advised to account for sky-condition composition differences to reduce estimation bias, and future work combining radiation-component observations with quantitative attribution models is needed to further reveal the core driving mechanisms.

4.3 Nonlinear environmental responses and their uncertainties

Across ecosystems, *NEE* showed stimulation-then-inhibition or saturation-type responses to *PAR*, *SWC*, *TA*, *TS* and *VPD*. Nevertheless, no statistically-significant turning point or clear critical threshold of *TA* was found for CMR. Response

https://doi.org/10.5194/egusphere-2026-6536
Preprint. Discussion started: 22 November 2026
© Author(s) 2026. CC BY 4.0 License.

thresholds obtained by statistical fitting varied substantially across ecosystems. These apparent breakpoints are sensitive to collinearity, sample distribution and bin width, and cannot be interpreted as physiological tolerance limits or optimal ecological ranges. Alpine carbon fluxes arise from multi-factor threshold constraints instead of single-factor linear controls; long-term stress adaptation amplifies spatial carbon-budget divergence. Climate warming and wetting disrupt wetland hydrothermal balance, accelerating deep soil carbon decomposition and CH_4 emissions and destabilizing its near-neutral carbon state. Wetland greenhouse gas budgets include CH_4 alongside CO_2, so N*EE*-only assessment carries inherent limitations (Song et al., 2021). The derived nonlinear response ranges support cross-comparison with published plateau threshold data, yet single-site extrapolation to regional scales requires caution.

4.4 Daytime, nighttime, and full-day driving mechanisms

Daytime *NEE* in all ecosystems was overwhelmingly dominated by *PAR*, corroborating the classic judgment that "energy limitation precedes water limitation" in alpine ecosystems (Sun et al., 2019). Secondary drivers diverged into three types—*TA* led temperature–moisture co-regulation (CMR), predominantly radiation-driven regime (ZLH), and multi-factor synergistic regulation led by *TA* (CDX) (Wang et al., 2021). The *SWC* exhibited the lowest explanatory power among all five factors during daytime, with composite scores of only 0.12–0.15 across all ecosystems. At night, dominant factors switched entirely to temperature-related variables, indicating strong temperature sensitivity of nocturnal carbon exchange. The three sites exhibited distinct regulatory patterns: coupled soil hydrothermal regulation (CDX), predominant soil-temperature control accompanied by elevated air temperature (CMR), and temperature-moisture synergistic regulation involving both atmospheric vapour and soil moisture (ZLH); the contributions of *SWC* increased by 2–3 times relative to daytime levels, while *VPD* contributions varied by ecosystem, correcting the simplified view that nighttime respiration is controlled by temperature alone. Full-day *NEE*, as intermediate integration between daytime and nighttime processes, exhibited driver-structure divergence determined by **t**he relative strength of daytime radiation control versus nighttime temperature control within each ecosystem: ecosystems where daytime radiation dominated overwhelmingly (e.g., ZLH, with daytime *PAR* is 0.88 and all-day *PAR* is 0.95) retained the simplest *PAR*-dominated all-day structure despite sharp diurnal switching, while ecosystems where non-*PAR* factors contributed more evenly across day and night exhibited the most balanced multi-factor driver structures (e.g., CDX, where non-*PAR* factors spanned only 0.14–0.31 in the all-day composite), cautioning against conclusion bias in ecosystems with sharp day–night switching when attributing full-period patterns. Furthermore, dominant meteorological drivers for alpine carbon exchange differ across temporal scales (Wang et al., 2023).

5 Limitations and future prospects

Owing to observational and design constraints, several limitations exist. First, the short flux time-series (less than four years) renders Mann–Kendall trends susceptible to interannual climatic noise; the changes of all ecosystems are only transient signals within the observation period, and the baseline for anomaly analysis has limited representativeness. Second, driver analyses relied on net *NEE* without separating *GPP* and ecosystem respiration, limiting mechanistic attribution to correlational inference. Lack of independent direct/diffuse radiation measurements means sky-type grouping mixes *TA*, *SWC* and *VPD* covariates, preventing isolation of diffuse-radiation effects. Third, identified thresholds are apparent breakpoints sensitive to collinearity and binning schemes. Although five weighting schemes (including the entropy weight method) produced consistent factor rankings, weighting assumptions may still influence composite scores, and three of the four analytical approaches are linear models with limited capacity to capture complex interactions. Fourth, one site per ecosystem type cannot fully separate vegetation-type effects from locational confounders (elevation, latitude, hydrology). Wetland carbon budgets include CH_4, so *NEE*-only assessments underestimate total climatic impacts (Huang et al., 2025;Song et al., 2021); freeze–thaw pulse emissions outside the growing season were not included.

https://doi.org/10.5194/egusphere-2026-6536
Preprint. Discussion started: 22 November 2026
© Author(s) 2026. CC BY 4.0 License.

To mitigate these shortcomings, future work should follow four directions. First, longer time series (≥ 5 year) will improve the robustness of trend and anomaly analyses. Second, partitioning *GPP* and respiration will disentangle photosynthetic and respiratory controls; radiation-partitioning models can retrieve direct and diffuse radiation to reduce covariate confounding. Third, multi-resolution binning and pre-emptive collinearity screening will refine breakpoint detection. Objective weighting (entropy weight, CRITIC) can replace subjective weights, and nonlinear models will better quantify synergistic and antagonistic factor interactions. Fourth, gradient sampling designs will separate site background from vegetation effects. Additional measurements of freeze–thaw and off-season carbon fluxes, together with CH_4 observations, will improve wetland carbon-sink evaluation.

6 Conclusions

Based on continuous flux observations of three typical ecosystems (alpine meadow, lakeside meadow, and alpine wetland) in the Three-River Headwaters region, this study clarified multi-scale *NEE* dynamics and their nonlinear environmental thresholds and driving mechanisms.

(1) Cloud cover strongly modulates alpine carbon exchange. The promotion of photosynthesis by diffuse radiation in alpine ecosystems was strongly light-intensity dependent: only within the moderate *PAR* range of 500–750 μmol·m^{-2}·s^{-1} was *NEE* significantly lower (i.e., stronger carbon uptake) on cloudy days than on sunny days in all three ecosystems. Nevertheless, the lack of separate direct and diffuse radiation measurements limits a definitive mechanistic attribution of this pattern.

(2) The three alpine ecosystems exhibited highly synchronized seasonal rhythms of *NEE*, all following a common pattern of a strong carbon sink in summer, a weak carbon sink in winter and transitional states in spring and autumn. Carbon-sink and carbon-release phases were broadly coherent across ecosystems, although ZLH reached its deepest sink earlier (April) than the regional July maximum. Carbon-sink magnitude and stability nevertheless showed substantial regional divergence: CMR had the strongest carbon sink, ZLH the highest stability, and CDX the largest proportion of carbon-source months. Collectively, these ecosystems shared convergent seasonal rhythms but divergent carbon-cycling functions.

(3) CMR and ZLH acted as persistent net carbon sinks throughout the observation period, whereas CDX was a net annual carbon source (0.11 μmol CO_2·m^{-2}·s^{-1};153.2 g C m^{-2}). No site showed a statistically significant unidirectional trend over the short record. Carbon-sink magnitude and fluctuation amplitude followed the gradients CMR > ZLH > CDX and CMR > CDX > ZLH, respectively. Source-strengthening (positive) anomalies dominated at CDX and ZLH, whereas CMR showed near-balanced anomalies with repeated late-summer sink-strengthening pulses, highlighting the modulation of alpine carbon budgets by growing-season hydrothermal variability.

(4) Environmental factors exerted pronounced nonlinear controls on *NEE*. Significant light-saturation points were detected for *PAR* (683.50–803.73 μmol·m^{-2}·s^{-1}), and statistically significant response thresholds were identified for *VPD* (391.99–440.92 Pa) and *TS* (9.61–11.45 °C) at all ecosystems. *SWC* breakpoints were identified at 0.08–0.35 m³/m³ but had very low explanatory power (R^2 ranging from 0.005–0.053). *TA* showed significant thresholds only at CDX and ZLH (10.67–12.87 °C, located at the lower end of the observed range); CMR failed the main quantile constraint and was classified as an edge breakpoint, although sensitivity tests suggested a threshold-type response close to the lower limit.

(5) A consistent day–night regulatory switch was identified across all three ecosystems: *PAR* dominates by day (0.85–0.88), *TS* by night (0.93–0.96), invariant across five weighting schemes (9/9). The sites differ only in secondary structure: CMR had the weakest daytime *PAR* control (0.85) but the strongest nocturnal *TS* control (0.96); CDX the most balanced all-day structure (non-*PAR* 0.14–0.31) with coupled soil hydrothermal regulation at night (*TS* 0.94; *SWC* 0.40; *VPD* 0.16); ZLH the strongest radiation control (daytime 0.88; all-day 0.95) but the weakest nocturnal *TS* control (0.93). *SWC* contributed least by day (0.12–0.15) yet became a secondary driver at night, so soil moisture modulates nocturnal carbon release far more than daytime uptake.

https://doi.org/10.5194/egusphere-2026-6536
Preprint. Discussion started: 22 November 2026
© Author(s) 2026. CC BY 4.0 License.

Appendix A

Table A1: Basic information of study sites

Site ID	Ecosystem type	Latitude and longitude	Altitude (m)	Dominant vegetation	Observation period
CMR	Alpine meadow	35.13°N,93.97°E	4462	Carex	2021-06-2024-04
CDX	Alpine Wetland	32.96°N, 94.18°E	4762	Kobresia peat marsh	2021-06-2025-03
ZLH	Lakeside meadow	35.12°N, 97.90°E	4281	Kobresia	2021-06-2025-03

Table A2: Statistics of sample size and gap proportion before and after flux quality control for each site

Index	CMR	CDX	ZLH
Total half-hourly records	49199	66203	65339
Valid non-missing records	36659	43654	46296
Total missing records	12540	22549	19043
Overall missing rate (%)	25.49	34.06	29.14
Total observation days	1031	1386	1370
Gap-free days	24 (2.3%)	4 (0.3%)	16 (1.2%)
Days with partial gaps	1007 (97.7%)	1382 (99.7%)	1354 (98.8%)
Days with complete gaps	0 (0.0%)	0 (0.0%)	0 (0.0%)
Maximum consecutive full-gap days	0	0	0
Number of independent gap segments	3690	4266	5340
Maximum gap duration (half-hourly points)	26	31	39
Maximum gap duration (hours)	13.0	15.5	19.5
Mean gap segment length (records)	3.4	5.3	3.6
Median gap segment length (records)	2	3	2
Fraction of single-point gaps (1 rec, 0.5h)	11.00%	5.91%	10.07%
Fraction of short gaps (2–6 recs, 1–3h)	46.33%	26.47%	44.40%
Fraction of moderate gaps (7–48 recs, 3.5h–1d)	42.66%	67.62%	45.53%

Table A3. Threshold regression results of relationships between NEE and environmental factors at the three Ecosystems(sen1)

Ecosystem	Factor	Unit	n	Breakpoint	95% CI	$Slope_1$	P_1	$Slope_2$	P_2	R^2	Breakpoint significant
CDX	SWC	m^3/m^3	14351	0.3539	[0.351, 0.363]	-4.0275	0	31.3069	0	0.0527	Yes
CDX	PAR	$\mu mol \cdot m^{-2} \cdot s^{-1}$	14351	804.3883	[695.558, 909.705]	-0.0066	0	-0.0006	0	0.2419	Yes
CDX	TA	°C	14297	10.667	[9.955, 11.818]	-0.3629	0	0.08	0.0204	0.0975	Yes
CDX	TS	°C	14336	10.3598	[9.978, 10.785]	-0.3246	0	-0.1472	0	0.0827	Yes
CDX	VPD	Pa	14194	403.8319	[362.646,	-0.0087	0	0.0001	0.7425	0.0638	Yes

https://doi.org/10.5194/egusphere-2026-6536
Preprint. Discussion started: 22 November 2026
© Author(s) 2026. CC BY 4.0 License.

					442.627]						
CMR	SWC	m³/m³	9874	0.164	[0.163, 0.191]	4.7699	0.2483	-19.417 4	0	0.0096	Yes
CMR	PAR	μmol·m⁻²·s⁻¹	9995	683.5027	[556.277, 873.761]	-0.0074	0	-0.0013	0	0.3494	Yes
CMR	TA	°C	9947	12.6024	[11.626, 13.325]	-0.3054	0	0.2027	0	0.1189	Yes
CMR	TS	°C	9995	9.6145	[8.982, 10.137]	-0.4008	0	0.1004	0	0.0729	Yes
CMR	VPD	Pa	9785	392.4215	[360.951, 441.093]	-0.0095	0	-0.0003	0.0345	0.0725	Yes
ZLH	SWC	m³/m³	13907	0.0802	[0.076, 0.090]	-13.205 4	0	2.604	0	0.0047	Yes
ZLH	PAR	μmol·m⁻²·s⁻¹	13907	715.014	[659.476, 786.695]	-0.0047	0	-0.0008	0	0.4217	Yes
ZLH	TA	°C	13849	12.8726	[11.819, 13.988]	-0.1415	0	0.0748	0	0.0663	Yes
ZLH	TS	°C	13907	11.448	[10.740, 12.342]	-0.1351	0	0.0713	0	0.0263	Yes
ZLH	VPD	Pa	13553	441.2519	[411.700, 473.017]	-0.005	0	-0.0002	0.0355	0.075	Yes

655 **Table A4. Threshold regression results of relationships between NEE and environmental factors at the three Ecosystems(sen2)**

Ecosystem	Factor	Unit	n	Breakpoint	95% CI	$Slope_1$	P_1	$Slope_2$	P_2	R^2	Breakpoint significant
CDX	SWC	m³/m³	14351	0.3538	[0.347, 0.365]	-4.042	0	31.2656	0	0.0527	Yes
CDX	PAR	μmol·m⁻²·s⁻¹	14351	802.7401	[691.224, 896.655]	-0.0067	0	-0.0006	0	0.2419	Yes
CDX	TA	°C	14297	10.667	[9.990, 11.683]	-0.3629	0	0.08	0.0204	0.0975	Yes
CDX	TS	°C	14336	10.3597	[9.839, 10.793]	-0.3246	0	-0.1472	0	0.0827	Yes
CDX	VPD	Pa	14194	403.8232	[368.101, 445.626]	-0.0087	0	0.0001	0.7425	0.0638	Yes
CMR	SWC	m³/m³	9874	0.164	[0.163, 0.191]	4.7699	0.2483	-19.4174	0	0.0096	Yes
CMR	PAR	μmol·m⁻²·s⁻¹	9995	683.503	[630.010, 865.509]	-0.0074	0	-0.0013	0	0.3494	Yes
CMR	TA	°C	9947	12.6021	[11.545, 13.056]	-0.3054	0	0.2026	0	0.1189	Yes
CMR	TS	°C	9995	9.61	[9.386, 10.143]	-0.401	0	0.1003	0	0.0729	Yes

https://doi.org/10.5194/egusphere-2026-6536
Preprint. Discussion started: 22 November 2026
© Author(s) 2026. CC BY 4.0 License.

CMR	VPD	Pa	9785	392.43	[355.682, 453.127]	-0.0095	0	-0.0003	0.0345	0.0725	Yes
ZLH	SWC	m^3/m^3	13907	0.0835	[0.076, 0.090]	-12.124	0	2.6872	0	0.0047	Yes
ZLH	PAR	$\mu mol \cdot m^{-2} \cdot s^{-1}$	13907	715.0048	[674.705, 760.783]	-0.0047	0	-0.0008	0	0.4217	Yes
ZLH	TA	°C	13849	12.8733	[11.662, 14.056]	-0.1414	0	0.0748	0	0.0663	Yes
ZLH	TS	°C	13907	11.448	[10.683, 12.429]	-0.1351	0	0.0713	0	0.0263	Yes
ZLH	VPD	Pa	13553	440.057	[410.772, 482.741]	-0.005	0	-0.0002	0.0321	0.075	Yes

Table A5：Weight coefficients under five weighting schemes

Weighting scheme	RF	PCA	MLR	COR
Subjective weighting	0.350	0.250	0.250	0.150
Entropy weight method	0.429	0.146	0.223	0.202
CRITIC method	0.229	0.341	0.230	0.200
Combined weighting	0.392	0.193	0.239	0.176
Equal weighting	0.250	0.250	0.250	0.250

Note: The Entropy weight method assigns the highest weight to RF (0.429) and the lowest weight to PCA (0.146), which is consistent with the expectation that more robust methods receive higher weights.

Table A6:Comparison of primary factor for each site-period under five weighting schemes

Site·Period	Subjective weighting	Entropy weight method	CRITIC	Combined weighting	Equal weighting	Consistency
CDX·Daytime	PAR	PAR	PAR	PAR	PAR	✓
CDX·All-day	PAR	PAR	PAR	PAR	PAR	✓
CDX·Night	TS	TS	TS	TS	TS	✓
CMR·Daytime	PAR	PAR	PAR	PAR	PAR	✓
CMR·All-day	PAR	PAR	PAR	PAR	PAR	✓
CMR·Night	TS	TS	TS	TS	TS	✓

https://doi.org/10.5194/egusphere-2026-6536
Preprint. Discussion started: 22 November 2026
© Author(s) 2026. CC BY 4.0 License.

Site·Period	Subjective weighting	Entropy weight method	CRITIC	Combined weighting	Equal weighting	Consistency
ZLH·Daytime	PAR	PAR	PAR	PAR	PAR	✓
ZLH·All-day	PAR	PAR	PAR	PAR	PAR	✓
ZLH·Night	TS	TS	TS	TS	TS	✓

Note: Among the nine site-period combinations, eight exhibited consistent primary factors across all five weighting schemes (9/9).

Table A7：Site·Period, Primary factor, Winning probability (%)

Site·Period	Primary factor	Winning probability (%)
CMR·Daytime	PAR	91.8
CMR·All-day	PAR	98.2
CMR·Night	TS	86.1
ZLH·Daytime	PAR	99.2
ZLH·All-day	PAR	100.0 (highest)
ZLH·Night	TS	89.6
CDX·Daytime	PAR	99.9
CDX·All-day	PAR	54.3 (lowest)
CDX·Night	TS	99.1
Mean	—	90.9

Table A8: Spearman's rank correlation matrix among weighting schemes

	Subjective weighting	Entropy weight method	CRITIC	Equal weighting
Subjective weighting	1.000	0.996	0.981	0.991
Entropy weight method	0.996	1.000	0.985	0.988
CRITIC	0.981	0.985	1.000	0.995
Equal weighting	0.991	0.988	0.995	1.000

https://doi.org/10.5194/egusphere-2026-6536
Preprint. Discussion started: 22 November 2026
© Author(s) 2026. CC BY 4.0 License.

Note: The Spearman rank correlations of 5 weighting schemes (the combined one excluded from the 4×4 matrix as an integrated derivative, all its correlations ≥ 0.985) are all ≥ 0.981, confirming high factor ranking consistency.

Code availability

All custom-written Python code used in this study — including the scripts for data quality control, gap filling, clearness-index-based sky-condition classification, piecewise-linear regression and bin-average analysis — is openly available on Zenodo at https://doi.org/10.5281/zenodo.23447137.

Data availability

The half-hourly eddy covariance *NEE* flux and environmental meteorological datasets used in this study are openly available on Zenodo at https://doi.org/10.5281/zenodo.23447984.

Author contributions

Shengchun Wang: Data curation, Investigation, Methodology, Software, Validation, Writing – original draft, Writing – review & editing, Formal analysis. Zhen Qiao: Conceptualization, Software, Methodology, Funding acquisition, Formal analysis, Writing – original draft. Wenwen Bai: Project administration, Resources, Supervision, Writing – review & editing. Wende A: Data curation, Formal analysis. Xin Li: Data curation, Formal analysis. Wenhui Li: Data curation, Formal analysis. Zhuolun He: Data curation, Formal analysis. Xinyimiao Zhang: Data curation, Formal analysis. Qingliang Zeng: Data curation, Formal analysis. Qinxia Zhao: Data curation, Formal analysis.

Competing interests

The contact author has declared that none of the authors has any competing interests.

Disclaimer

Copernicus Publications adds a standard disclaimer: “Copernicus Publications remains neutral with regard to jurisdictional claims made in the text, published maps, institutional affiliations, or any other geographical representation in this paper. While Copernicus Publications makes every effort to include appropriate place names, the final responsibility lies with the authors. Views expressed in the text are those of the authors and do not necessarily reflect the views of the publisher.”
Please feel free to add disclaimer text at your choice, if applicable.

Acknowledgements

The authors thank the field teams maintaining the eddy covariance stations at Chumar River (CMR), Zhaling Lake (ZLH) and Chadan (CDX) for their long-term efforts in site operation, instrument maintenance and in-situ observations. This work makes

https://doi.org/10.5194/egusphere-2026-6536
Preprint. Discussion started: 22 November 2026
© Author(s) 2026. CC BY 4.0 License.

use of the flux observation infrastructure within the Three-River Headwaters region. We acknowledge Zenodo for hosting the archived dataset and analysis code.

Financial support

This research has been supported by the National Key Research and Development Program of China (grant no. 2023YFC3206301), the Key Research and Development Program of Ningxia Hui Autonomous Region (grant no. 2024BEG02034), the Self-Proposed Project of the Key Laboratory of Water Ecological Governance and Protection in River Source Region, Ministry of Water Resources, and the Youth Innovation Talent Cultivation Program of Qinghai University for Enhancing Scientific Research Capacity (grant no. 4211020322).

Review statement

The review statement will be added by Copernicus Publications listing the handling editor as well as all contributing referees according to their status anonymous or identified.

References

Abdaki, M., Sanchez-Azofeifa, A., and Hamann, H. F.: A machine learning approach for filling long gaps in eddy covariance time series data in a tropical dry forest, J. Geophys. Res.-Biogeo., 130, e2024JG008375, https://doi.org/10.1029/2024JG008375, 2025.

Aubinet, M., Vesala, T., and Papale, D. (Eds.): Eddy covariance: a practical guide to measurement and data analysis, Springer, Dordrecht, https://doi.org/10.1007/978-94-007-2351-1, 2012.

Baldocchi, D. D.: Assessing the eddy covariance technique for evaluating carbon dioxide exchange rates of ecosystems: past, present and future, Glob. Change Biol., 9, 479–492, https://doi.org/10.1046/j.1365-2486.2003.00629.x, 2003.

Chai, X., Li, Y. N., Duan, C., Zhang, T., Zong, N., Shi, P. L., He, Y. T., and Zhang, X. Z.: CO_2 flux dynamics and limiting factors of alpine shrub meadow and steppe meadow on the Qinghai-Tibet Plateau, Chin. J. Plant Ecol., 42, 6–19, https://doi.org/10.17521/cjpe.2017.0266, 2018.

Chapin, F. S., III, Matson, P. A., and Mooney, H. A.: Principles of terrestrial ecosystem ecology, Springer, Dordrecht, https://doi.org/10.1007/b97397, 2002.

Chen, D. L., Xu, B. Q., and Yao, T. D.: Assessment of past, present and future environmental changes on the Tibetan Plateau, Chin. Sci. Bull., 60, 3025–3035, https://doi.org/10.1360/n972014-01370, 2015.

Chen, H., Ju, P., Zhu, Q., Xu, X., Wu, N., Gao, Y., Feng, X., Tian, J., Niu, S., Zhang, Y., Peng, C., and Wang, Y.: Carbon and nitrogen cycling on the Qinghai–Tibetan Plateau, Nat. Rev. Earth Environ., 3, 701–716, https://doi.org/10.1038/s43017-022-00344-2, 2022.

Chen, Z. G., Zhang, X., Liu, X. Q., Zhang, L. F., Tang, Y. H., Du, M. Y., and Gu, S.: Response of net ecosystem carbon exchange to diffuse radiation changes in an alpine meadow of the Qinghai-Tibet Plateau, Chin. J. Appl. Ecol., 29, 1829–1838, https://doi.org/10.13287/j.1001-9332.201806.002, 2018.

Chu, X. J., Han, G. X., and Xing, Q. H.: Effects of cloudy and sunny days on net ecosystem CO_2 exchange of reed wetland in the Yellow River Delta, Chin. J. Plant Ecol., 39, 661–673, https://doi.org/10.17521/cjpe.2015.0063, 2015.

https://doi.org/10.5194/egusphere-2026-6536
Preprint. Discussion started: 22 November 2026
© Author(s) 2026. CC BY 4.0 License.

Ding, J., Li, F., Yang, G., Chen, L., Zhang, B., Liu, L., Fang, K., Qin, S., Chen, Y., Peng, Y., Ji, C., He, H., Smith, P., and Yang, Y.: The permafrost carbon inventory on the Tibetan Plateau: a new evaluation using deep sediment cores, Glob. Change Biol., 22, 2688–2701, https://doi.org/10.1111/gcb.13257, 2016.

Duan, C. W., Li, X. L., and Li, C. Y.: Formation mechanism of bare patches and key limiting factors for ecological restoration in alpine meadows of the Yellow River source region, Acta Ecol. Sin., 44, 6952–6964, https://doi.org/10.20103/j.stxb.202308051674, 2024.

Falge, E., Baldocchi, D., Olson, R., Anthoni, P., Aubinet, M., Bernhofer, C., Burba, G., Ceulemans, R., Clement, R., Dolman, H., Granier, A., Gross, P., Grünwald, T., Hollinger, D., Jensen, N.-O., Katul, G., Keronen, P., Kowalski, A., Lai, C. T., Law, B. E., Meyers, T., Moncrieff, J., Moors, E., Munger, J. W., Pilegaard, K., Rannik, Ü., Rebmann, C., Suyker, A., Tenhunen, J., Tu, K., Verma, S., Vesala, T., Wilson, K., Wofsy, S.: Gap filling strategies for defensible annual sums of net ecosystem exchange, Agric. For. Meteorol., 107, 43–69, https://doi.org/10.1016/S0168-1923(00)00225-2, 2001.

Fang, J. Y., Tang, Y. H., and Son, Y.: Why are East Asian ecosystems important for carbon cycle research?, Sci. China Life Sci., 53, 753–756, https://doi.org/10.1007/s11427-010-4032-2, 2010.

Foken, T., Leuning, R., Oncley, S. R., Mauder, M., and Aubinet, M.: Corrections and data quality control, in: Eddy Covariance: A Practical Guide to Measurement and Data Analysis, edited by: Aubinet, M., Vesala, T., and Papale, D., Springer, Dordrecht, 85–131, https://doi.org/10.1007/978-94-007-2351-1_4, 2012.

Geng, X. D. and Xu, R.: Effects of gradient warming on ecosystem carbon exchange in an alpine meadow of the Qinghai-Tibet Plateau, Pratacult. Sci., 34, 2407–2415, https://doi.org/10.11829/j.issn.1001-0629.2017-0074, 2017.

Greco, S., Ishizaka, A., Tasiou, M., and Torrisi, G.: On the methodological framework of composite indices: a review of the issues of weighting, aggregation, and robustness, Soc. Indic. Res., 141, 61–94, https://doi.org/10.1007/s11205-017-1832-9, 2019.

Gu, L., Baldocchi, D. D., Verma, S. B., Black, T. A., Vesala, T., Falge, E. M., and Dowty, P. R.: Advantages of diffuse radiation for terrestrial ecosystem productivity, J. Geophys. Res.-Atmos., 107(D6), ACL2-1–ACL2-23, https://doi.org/10.1029/2001JD001242, 2002.

Gu, S., Tang, Y. H., Du, M. Y., Kato, T., Li, Y. N., Cui, X. Y., and Zhao, X. Q.: Short-term variation of CO_2 flux in relation to environmental controls in an alpine meadow on the Qinghai-Tibetan Plateau, J. Geophys. Res.-Atmos., 108, 4670, https://doi.org/10.1029/2003JD003584, 2003.

Han, P., Lin, X., Zhang, W., Wang, G., and Wang, Y.: Projected changes of alpine grassland carbon dynamics in response to climate change and elevated CO_2 concentrations under Representative Concentrations Pathways (RCP) scenarios, PLOS ONE, 14, e0215261, https://doi.org/10.1371/journal.pone.0215261, 2019.

He, F. Q., Li, Q., Chen, D. D., Luo, C. Y., Zhang, Y. K., Zhang, L., Pan, S. C., Zhao, Z. J., and Zhao, L.: Water availability regulates the carbon uptake period and amplitude of net ecosystem exchange in alpine grasslands of the Qinghai-Xizang Plateau, Agric. For. Meteorol., 372, 110656, https://doi.org/10.1016/j.agrformet.2025.110656, 2025.

He, H. D., Li, H. Q., Zhu, J. B., Zhang, F. W., and Yang, Y. S.: Seasonal and interannual dynamics of ecosystem respiration and its influencing factors in alpine wetlands in the Qilian Mountains, Acta Ecol. Sin., 42, 5956–5965, https://doi.org/10.5846/stxb202108172274, 2022.

Hou, Q., Gao, Z., Duan, Z., and Yu, M.: Interpolating turbulent heat fluxes missing from a prairie observation on the Tibetan Plateau using artificial intelligence models, Geosci. Model Dev., 18, 4625–4641, https://doi.org/10.5194/gmd-18-4625-2025, 2025.

Huang, J., Zhou, X., Wu, G., Xu, X., Zhao, Q., Liu, Y., Duan, A., Xie, Y., Ma, Y., Zhao, P., Yang, S., Yang, K., Yang, H., Bian, J., Fu, Y., Ge, J., Liu, Y., Wu, Q., Yu, H., Wang, B., Bao, Q., and Qie, K.: Global climate impacts of land-surface and atmospheric processes over the Tibetan Plateau, Rev. Geophys., 61, e2022RG000771, https://doi.org/10.1029/2022RG000771, 2023.

https://doi.org/10.5194/egusphere-2026-6536
Preprint. Discussion started: 22 November 2026
© Author(s) 2026. CC BY 4.0 License.

Huang, L., Qin, S., Kou, D., Ciais, P., Xu, X., Peñuelas, J., Xi, Y., Yang, G., Song, Y., Yao, S., Chang, J., and Yang, Y.: Spatiotemporal patterns of methane fluxes across alpine permafrost region on the Tibetan Plateau, Nat. Commun., 16, 7474, https://doi.org/10.1038/s41467-025-62699-6, 2025.

Jekel, C. F. and Venter, G.: pwlf: A Python Library for Fitting 1D Continuous Piecewise Linear Functions, https://github.com/cjekel/piecewise_linear_fit_py, 2019.

Li, C. Y., Liang, Y. T., Wang, B. B., Cai, M. Y., Liu, Q., Lai, C. M., Sun, J. B., and Peng, F.: Plant and soil stoichiometric characteristics of degraded alpine meadows in the Yangtze River source region, Pratacult. Sci., 41, 1029–1038, 2024.

Li, S. G., Asanuma, J., Eugster, W., Kotani, A., Liu, J. J., Urano, T., Oikawa, T., Davaa, G., Oyunbaatar, D., and Sugita, M.: Net ecosystem carbon dioxide exchange over grazed steppe in central Mongolia, Glob. Change Biol., 11, 1941–1955, https://doi.org/10.1111/j.1365-2486.2005.01047.x, 2005.

Li, W. J., Li, W. L., Xiong, Y. C., Luo, Q., and Wang, W. Y.: Spatiotemporal evolution and influencing factors of vegetation NPP in the Three-River Headwaters region from 2000 to 2023, Acta Agrestia Sin., 33, 3003–3013, https://doi.org/10.11733/j.issn.1007-0435.2025.09.024, 2025.

Li, Y., Ganjurjav, H., Hu, G. Z., Wan, Y. F., Li, Y. E., Danjiu, L. B., He, S. C., Xie, W. D., and Gao, Q. Z.: Effects of warming on respiration in an alpine meadow of the Qinghai-Tibet Plateau, Acta Ecol. Sin., 40, 266–273, https://doi.org/10.5846/stxb201811302609, 2020.

Li, Z. G., Lyu, S. H., and Ao, Y. H.: Analysis of summer micrometeorological characteristics and carbon flux variation in the near-surface layer of the Ngoring Lake lakeside area, Prog. Geogr., 31, 602–608, https://doi.org/10.11820/dlkxjz.2012.05.008, 2012.

Liang, C. and Zhu, X. F.: The soil microbial carbon pump as a new concept for terrestrial carbon sequestration, Sci. China Earth Sci., 64, 545–558, https://doi.org/10.1007/s11430-020-9705-9, 2021.

Liu, H. Z., Du, Q., Xu, L. J., Liu, Y., Meng, X. N., Shao, Y. M., and Zheng, Y. Q.: Patterns of Carbon and water exchange characteristics of different ecosystems on the southeastern Qinghai-Tibet Plateau, Chin. J. Atmos. Sci., 48, 188–199, https://doi.org/10.3878/j.issn.1006-9895.2309.23315, 2024.

Liu, J., Tong, X. J., Zhang, J. S., Meng, P., Li, J., and Zheng, N.: Effects of solar radiation on net ecosystem carbon exchange in an artificial mixed forest at Xiaolangdi, Yellow River, Acta Ecol. Sin., 34, 2118–2127, https://doi.org/10.5846/stxb201308182105, 2014.

Muggeo, V. M. R.: Estimating regression models with unknown break-points, Stat. Med., 22, 3055–3071, https://doi.org/10.1002/sim.1545, 2003.

Novick, K. A., Ficklin, D. L., Stoy, P. C., Williams, C. A., Bohrer, G., Oishi, A. C., Papuga, S. A., Blanken, P. D., Noormets, A., Sulman, B. N., Scott, R. L., Wang, L., and Phillips, R. P.: The increasing importance of atmospheric demand for ecosystem water and carbon fluxes, Nat. Clim. Change, 6(11), 1023–1027, https://doi.org/10.1038/nclimate3114, 2016.

Pepin, N., Bradley, R. S., Diaz, H. F., Baraer, M., Caceres, E. B., Forsythe, N., Fowler, H., Greenwood, G., Hashmi, M. Z., Liu, X. D., Miller, J. R., Ning, L., Ohmura, A., Palazzi, E., Rangwala, I., Schöner, W., Severskiy, I., Shahgedanova, M., Wang, M. B., Williamson, S. N., and Yang, D. Q.: Elevation-dependent warming in mountain regions of the world, Nat. Clim. Change, 5, 424–430, https://doi.org/10.1038/nclimate2563, 2015.

Pianosi, F., Beven, K., Freer, J., Hall, J. W., Rougier, J., Stephenson, D. B., and Wagener, T.: Sensitivity analysis of environmental models: a systematic review with practical workflow, Environ. Model. Softw., 79, 214–232, https://doi.org/10.1016/j.envsoft.2016.02.008, 2016.

Pillai, N. D., Wille, C., Nieberding, F., Helbig, M., and Sachs, T.: A year-long eddy covariance dataset over an Alpine Steppe on the central Tibetan Plateau: a landscape perspective on carbon and energy fluxes, Earth Syst. Sci. Data, 18(7), 5627–5641, https://doi.org/10.5194/essd-18-5627-2026, 2026.

https://doi.org/10.5194/egusphere-2026-6536
Preprint. Discussion started: 22 November 2026
© Author(s) 2026. CC BY 4.0 License.

Qian, Q., Zhang, X. J., and Wang, J. B.: Spatiotemporal patterns of grassland livestock carrying capacity in the Three-River Headwaters region from 2005 to 2017, Acta Agrestia Sin., 29, 1311–1317, https://doi.org/10.11733/j.issn.1007-0435.2021.06.022, 2021.

Reichstein, M., Tenhunen, J. D., Roupsard, O., Ourcival, J. M., Rambal, S., Miglietta, F., Peressotti, A., Pecchiari, M., Tirone, G., and Valentini, R.: Severe drought effects on ecosystem CO_2 and H_2O fluxes at three Mediterranean evergreen sites: revision of current hypotheses, Glob. Change Biol., 8, 999–1017, https://doi.org/10.1046/j.1365-2486.2002.00530.x, 2002.

Ren, X. L., He, H. L., and Zhang, L.: Effects of diffuse radiation on gross primary productivity simulation of alpine grassland on the Qinghai-Tibet Plateau, Res. Environ. Sci., 30, 1898–1907, https://doi.org/10.13198/j.issn.1001-6929.2017.02.26, 2017.

Shi, S. B., Shang, Y. X., and Zhu, P. J.: Photosynthetic physiological characteristics of several alpine plants on the Qinghai-Tibet Plateau, Acta Bot. Boreal.-Occident. Sin., 33, 1175–1181, https://doi.org/10.3969/j.issn.1000-4025.2013.06.012, 2013.

Schädel, C., Bader, M. K.-F., Schuur, E. A. G., Biasi, C., Bracho, R., Čapek, P., De Baets, S., Diáková, K., Ernakovich, J., Estop-Aragones, C., Graham, D. E., Hartley, I. P., Iversen, C. M., Kane, E., Knoblauch, C., Lupascu, M., Martikainen, P. J., Natali, S. M., Norby, R. J., O'Donnell, J. A., Roy Chowdhury, T., Šantrůčková, H., Shaver, G., Sloan, V. L., Treat, C. C., Turetsky, M. R., Waldrop, M. P., and Wickland, K. P.: Potential carbon emissions dominated by carbon dioxide from thawed permafrost soils, Nat. Clim. Change, 6(10), 950–953, https://doi.org/10.1038/nclimate3054, 2016.

Souza, R. P., Machado, E. C., Silva, J. A. B., Lagôa, A. M. M. A., and Silveira, J. A. G.: Photosynthetic gas exchange, chlorophyll fluorescence and some associated metabolic changes in cowpea (Vigna unguiculata) during water stress and recovery, Environ. Exp. Bot., 51, 45–56, https://doi.org/10.1016/S0098-8472(03)00059-5, 2004.

Song, W., Wang, H., Wang, G., Chen, L., Jin, Z., Bramley, H., and Zhang, F.: Methane emissions during different freezing-thawing periods from a fen on the Qinghai-Tibetan Plateau: Four years of measurements, Agric. For. Meteorol., 297, 108279, https://doi.org/10.1016/j.agrformet.2020.108279, 2021.

Sun, H., Cao, Y. Q., Chen, J. M., Zhang, Y., Wang, S. X., Wang, J. Q., Zhang, W., Lei, J. F., Huang, Q. C., Zhou, Q. P., and Hu, J.: Carbon pool characteristics and influencing factors of a typical alpine wetland in Zoige, National Park, 3, 141–153, https://doi.org/10.20152/j.np.202412250135, 2025.

Sun, H. L., Zheng, D., Yao, T. D., and Zhang, Y. L.: Protection and construction of the national ecological security shelter zone on the Tibetan Plateau, Acta Geogr. Sin., 67, 3–12, https://doi.org/10.11821/xb201201001, 2012.

Sun, S. B., Che, T., Li, H. Y., Wang, T. J., Ma, C. F., Liu, B., Wu, Y. T., and Song, Z. L.: Water and carbon dioxide exchange of an alpine meadow ecosystem in the northeastern Tibetan Plateau is energy-limited, Agric. For. Meteorol., 275, 283–295, https://doi.org/10.1016/j.agrformet.2019.06.003, 2019.

Sun, S. B., Che, T., and Gentine, P.: Shallow groundwater inhibits soil respiration and favors carbon uptake in a wet alpine meadow ecosystem, Agric. For. Meteorol., 297, 108254, https://doi.org/10.1016/j.agrformet.2020.108254, 2021.

Toms, J. D. and Lesperance, M. L.: Piecewise regression: a tool for identifying ecological thresholds, Ecology, 84, 2034–2041, https://doi.org/10.1890/02-0472, 2003.

Wang, B. and Piao, S. L.: Estimate of terrestrial carbon balance over the Tibetan Plateau: progresses, challenges and perspectives, Quat. Sci., 43, 313–323, https://doi.org/10.11928/j.issn.1001-7410.2023.02.01, 2023.

Wang, B., Jin, H., Li, Q., Chen, D., Zhao, L., Tang, Y., Kato, T., and Gu, S.: Diurnal and seasonal variations in the net ecosystem CO_2 exchange of a pasture in the three river source region of the Qinghai-Tibetan Plateau, PLOS ONE, 12, e0170963, https://doi.org/10.1371/journal.pone.0170963, 2017.

Wang, S., Zhang, Y., Lü, S., Su, P., Shang, L., and Li, Z.: Biophysical regulation of carbon fluxes over an alpine meadow ecosystem in the eastern Tibetan Plateau, Int. J. Biometeorol., 60(6), 801–812, https://doi.org/10.1007/s00484-015-1074-y, 2016.

https://doi.org/10.5194/egusphere-2026-6536
Preprint. Discussion started: 22 November 2026
© Author(s) 2026. CC BY 4.0 License.

Wang, S., Zhang, Y., Meng, X., Shang, L., Li, Z., and Li, S.: Water availability control the seasonal and inter-annual variability of CO_2 fluxes in an alpine meadow on the eastern Tibetan Plateau, Agric. For. Meteorol., 356, 110187, https://doi.org/10.1016/j.agrformet.2024.110187, 2024.

Wang, X. Y., Zhou, B. R., Su, S. L., Zhou, H. K., Du, H. L., and Zhang, R.: Carbon exchange characteristics and meteorological influencing mechanisms of alpine meadow and desert in the Qinghai-Tibet Plateau, Acta Ecol. Sin., 43, 1194–1208, https://doi.org/10.5846/stxb202112303709, 2023.

Wang, Y., Xiao, J., Ma, Y., Ding, J., Chen, X., Ding, Z., and Luo, Y.: Persistent and enhanced carbon sequestration capacity of alpine grasslands on Earth's Third Pole, Sci. Adv., 9(20), eade6875, https://doi.org/10.1126/sciadv.ade6875, 2023.

Wang, Y. Y., Xiao, J. F., Ma, Y. M., Luo, Y. Q., Hu, Z. Y., Li, F., Li, Y. N., Gu, L. L., Li, Z. G., and Yuan, L.: Carbon fluxes and environmental controls across different alpine grassland types on the Tibetan Plateau, Agric. For. Meteorol., 311, 108694, https://doi.org/10.1016/j.agrformet.2021.108694, 2021.

Wei, D., Qi, Y. H., Ma, Y. M., Wang, X. F., Ma, W. Q., Gao, T. G., Huang, L., Zhao, H., Zhang, J. X., and Wang, X. D.: Plant uptake of CO_2 outpaces losses from permafrost and plant respiration on the Tibetan Plateau, Proc. Natl. Acad. Sci. USA, 118, e2015283118, https://doi.org/10.1073/pnas.2015283118, 2021.

Wei, J., Li, X., Liu, L., Christensen, T. R., Jiang, Z., Ma, Y., Wu, X., Yao, H., and López-Blanco, E.: Radiation, soil water content, and temperature effects on carbon cycling in an alpine swamp meadow of the northeastern Qinghai–Tibetan Plateau, Biogeosciences, 19, 861–875, https://doi.org/10.5194/bg-19-861-2022, 2022.

Weng, B. S., Dong, Z. Y., Yang, Y. H., Yan, D. H., Li, M. Y., and Zhang, Y. H.: Effects of warming and increased precipitation on soil microbial residues on the Qinghai-Tibet alpine meadows, EGUsphere [preprint], https://doi.org/10.5194/egusphere-2022-1290, 2022.

Wu, L. B., Gu, S., Zhao, L., Xu, S. X., Zhou, H. K., Feng, C., Xu, W. X., Li, Y. N., Zhao, X. Q., and Tang, Y. H.: Net ecosystem CO_2 exchange, gross primary productivity and their influencing factors in artificial grassland in the Three-River Headwaters region, Chin. J. Plant Ecol., 34, 770–780, https://doi.org/10.3773/j.issn.1005-264x.2010.07.002, 2010.

Wutzler, T., Lucas-Moffat, A., Migliavacca, M., Knauer, J., Sickel, K., Šigut, L., Menzer, O., and Reichstein, M.: Basic and extensible post-processing of eddy covariance flux data with REddyProc, Biogeosciences, 15, 5015–5030, https://doi.org/10.5194/bg-15-5015-2018, 2018.

Xiao, J., Baldocchi, D., Ichii, K., Li, F., and Papale, D.: Insights into terrestrial carbon and water cycling from the global eddy covariance network, Nat. Rev. Earth Environ., 7, 60–79, https://doi.org/10.1038/s43017-025-00743-1, 2026.

Xie, J., Chen, J., Sun, G., Chu, H., Noormets, A., Ouyang, Z., John, R., and Wan, S.: Long-term variability and environmental control of the carbon cycle in an oak-dominated temperate forest, For. Ecol. Manage., 313, 319–328, https://doi.org/10.1016/j.foreco.2013.10.032, 2014.

Xie, Q. L., Yang, X., and Hao, L. N.: Spatiotemporal variation characteristics and influencing factors of vegetation coverage in the Three-River Headwaters region from 2001 to 2020, Bull. Soil Water Conserv., 42, 202–212, https://doi.org/10.13961/j.cnki.stbctb.20221017.001, 2022.

Jung, M., Reichstein, M., Schwalm, C. R., Huntingford, C., Sitch, S., Ahlström, A., Arneth, A., Camps-Valls, G., Ciais, P., Friedlingstein, P., Gans, F., Ichii, K., Jain, A. K., Kato, E., Papale, D., Poulter, B., Raduly, B., Rödenbeck, C., Tramontana, G., Viovy, N., Wang, Y.-P., Weber, U., Zaehle, S., and Zeng, N.: Compensatory water effects link yearly global land CO_2 sink changes to temperature, Nature, 541(7638), 516–520, https://doi.org/10.1038/nature20780, 2017.

Xu, M., Sun, Y., Zhang, T., Zhang, Y., Zhu, J., He, Y., Wang, L., and Yu, G.: Biotic effects dominate the inter-annual variability in ecosystem carbon exchange in a Tibetan alpine meadow, J. Plant Ecol., 15, 882–896, https://doi.org/10.1093/jpe/rtac005, 2022.

https://doi.org/10.5194/egusphere-2026-6536
Preprint. Discussion started: 22 November 2026
© Author(s) 2026. CC BY 4.0 License.

Yang, T. W., Sun, J. J., Li, Y. F., Wang, M., Li, H. K., Wang, S. Z., Xia, Z. Y., and Yu, Z. C.: Impact of climate-induced water-table drawdown on carbon and nitrogen sequestration in a Kobresia-dominated peatland on the central Qinghai-Tibetan Plateau, Commun. Earth Environ., 6, 188, https://doi.org/10.1038/s43247-025-02168-6, 2025.

Yao, T. D., Xue, Y. K., Chen, D. L., Chen, F. H., Thompson, L., Cui, P., Koike, T., Lau, W. K.-M., Lettenmaier, D., Mosbrugger, V., Zhang, R. H., Xu, B. Q., Dozier, J., Gillespie, T., Gu, Y., Kang, S. C., Piao, S. L., Sugimoto, S., Ueno, K., Wang, L., Wang, W. C., Zhang, F., Sheng, Y. W., Guo, W. D., Ailikun, Yang, X. X., Ma, Y. M., Shen, S. S. P., Su, Z. B., Chen, F., Liang, S. L., Liu, Y. M., Singh, V. P., Yang, K., Yang, D. Q., Zhao, X. Q., Qian, Y., Zhang, Y., and Li, Q.: Recent third pole's rapid warming accompanies cryospheric melt and water cycle intensification and interactions between monsoon and environment: multidisciplinary approach with observations, modeling, and analysis, Bull. Am. Meteorol. Soc., 100, 423–444, https://doi.org/10.1175/BAMS-D-17-0057.1, 2019.

Yao, T. D., Bolch, T., Chen, D., Gao, J., Immerzeel, W., Piao, S., Su, F., Thompson, L., Wada, Y., Wang, L., Wang, T., Wu, G., Xu, B., Yang, W., Zhang, G., and Zhao, P.: The imbalance of the Asian water tower, Nat. Rev. Earth Environ., 3, 618–632, https://doi.org/10.1038/s43017-022-00299-4, 2022.

Zeng, N., Ren, X. L., and He, H. L.: Spatiotemporal dynamics of above-ground biomass and its climatic drivers in Three-River Source Region National Park, Acta Ecol. Sin., 43, 1175–1184, https://doi.org/10.5846/stxb202112163570, 2023.

Zhang, F. W., Li, Y. N., Cao, G. M., and Zhao, X. Q.: CO_2 flux characteristics and driving factors of alpine meadow steppe on the north shore of Qinghai Lake, Chin. J. Plant Ecol., 36, 187–198, https://doi.org/10.3724/SP.J.1258.2012.00187, 2012.

Zhang, Y. Y., Liu, M. X., Pan, J. H., Chen, X. J., Chen, Y. Y., and Zhang, X.: Spatiotemporal patterns and dynamic simulation of carbon budget in alpine meadows of Gannan, Acta Ecol. Sin., 44, 5542–5553, https://doi.org/10.20103/j.stxb.202401160140, 2024.

Zhang, Z. L., Zhou, Y., Jiang, J., Wang, L. N., Deng, X., An, Z. C., and Tang, Y. K.: Simulation and influencing mechanisms of carbon and water fluxes in Artemisia sacrorum grassland on the Loess Plateau based on an ecological knowledge-machine learning model, Acta Ecol. Sin., 45, 6544–6558, https://doi.org/10.20103/j.stxb.202409132223, 2025.

Zhang, Z. Q., Cai, H. W., and Zhang, P. P.: Spatiotemporal variations of vegetation carbon source and sink in the Three-River Headwaters region based on GEE remote sensing platform, Remote Sens. Land Resour., 35, 231–242, https://doi.org/10.6046/zrzyyg.2022042, 2023.

Zhao, L., Li, Y. N., Xu, S. X., Zhou, H. K., Gu, S., Yu, G. R., and Zhao, X. Q.: Diurnal, seasonal and annual variation in net ecosystem CO_2 exchange of an alpine shrubland on Qinghai-Tibetan Plateau, Glob. Change Biol., 12, 1940–1953, https://doi.org/10.1111/j.1365-2486.2006.01197.x, 2006.

Wang, S.: Code for "Spatiotemporal Dynamics and Environmental Drivers of CO_2 Fluxes in Typical Qinghai–Tibet Alpine Ecosystems", Zenodo [code], https://doi.org/10.5281/zenodo.23447137, 2026a.

Wang, S: Eddy covariance CO_2 flux and meteorological dataset of typical alpine ecosystems in the Three-River Headwaters Region (2021–2025), Zenodo [dataset], https://doi.org/10.5281/zenodo.23447984, 2026b.